



**OPTIMIZATION OF DETECTOR PLACEMENT FOR HIDDEN RADIATION SOURCE  
DETECTION**

THESIS

Michael E. Morrison, Major, USA

AFIT-ENP-MS-15-M-082

**DEPARTMENT OF THE AIR FORCE  
AIR UNIVERSITY**

*AIR FORCE INSTITUTE OF TECHNOLOGY*

---

---

**Wright-Patterson Air Force Base, Ohio**

**DISTRIBUTION STATEMENT A.  
APPROVED FOR PUBLIC RELEASE; DISTRIBUTION UNLIMITED**

The views expressed in this thesis are those of the author and do not reflect the official policy or position of the United States Air Force, Department of Defense, or the United States Government. This material is declared a work of the U.S. Government and is not subject to copyright protection in the United States.

OPTIMIZATION OF DETECTOR PLACEMENT FOR HIDDEN RADIATION SOURCE  
DETECTION

THESIS

Presented to the Faculty  
Department of Engineering Physics  
Graduate School of Engineering and Management  
Air Force Institute of Technology  
Air University  
Air Education and Training Command  
In Partial Fulfillment of the Requirements for the  
Degree of Master of Science in Nuclear Engineering

Michael E. Morrison, BS

Major, USA

March 2015

**DISTRIBUTION STATEMENT A.**

**APPROVED FOR PUBLIC RELEASE; DISTRIBUTION UNLIMITED**

OPTIMIZATION OF DETECTOR PLACEMENT FOR HIDDEN RADIATION SOURCE  
DETECTION

Michael E. Morrison, BS

Major, USA

Committee Membership:

Dr. J. A. Clinton

Chair

Dr. J. W. McClory

Member

Maj B. J. Singleton

Member

## Abstract

This research validated a 2-D photon attenuation analytical transport model designed to determine optimal placement of multiple gamma detectors and compared the results of the model to a Monte Carlo n-Particle (MCNP) simulation. The 2-D attenuation model is able to predict optimal detector locations with the same proficiency as the MCNP simulation in approximately 1/168<sup>th</sup> of the time using the same computing hardware and with comparable accuracy. The MCNP model took 14 hours to complete the calculation where the 2-D attenuation model only took 5 minutes. Since faster predictions are important in achieving operationally useful methods for optimizing detector emplacement, the 2-D attenuation model approach promises to speed up the process of hidden source detection significantly. The model focused on detection of the full energy peak of a radiation source. Methods to optimize detector placement for scattered radiation are described but require further development. The model developed in this research is designed to enable fast determination of the optimal placement of detectors to acquire a radiation source using input parameters acquired from polarimetric-hyperspectral imagery.

## Acknowledgements

I would like to express my sincere appreciation to my faculty advisor, Dr. Justin Clinton, for his guidance and support throughout the course of this thesis effort. The insight and experience was certainly appreciated. I would, also like to thank LTC Stephen McHale, and MAJ Briana Singleton for their continuous presence and assistance with this project.

Michael Morrison

## Table of Contents

	Page
Abstract .....	iv
Acknowledgements .....	v
Table of Contents .....	vi
List of Figures .....	viii
List of Tables .....	xi
I. Introduction .....	12
1.1 Relevance of work .....	12
1.2 Hypothesis .....	3
II. Theory .....	5
2.1 Chapter Overview .....	5
2.2 Gamma Radiation .....	5
2.2.1 Attenuation .....	6
2.2.1.1 Photoelectric Effect .....	7
2.2.1.2 Compton Scattering .....	8
2.3 Gamma Detection .....	10
2.3.1 Detector Characteristics .....	10
2.3.2 Types of Detectors .....	13
2.3.2.1 Scintillators .....	13
2.3.2.2 Semiconductor Detectors .....	15
2.4 Gamma Spectroscopy .....	15
2.4.1 The Compton Edge and the Compton Continuum .....	16
2.4.2 Backscatter Peak .....	17
2.4.3 Background and Minimum Detectable Activity .....	18
III. Methodology .....	19
3.1 Chapter Overview .....	19
3.2 MCNP .....	19
3.2.1 F4 tally (MCNP) .....	21

3.2.2	Simulation Setup.....	22
3.3	Experimental Setup .....	23
3.3.1	Data Collection .....	24
3.4	Statistics .....	25
3.5	Analytical model in 2-D.....	27
3.6	Multi Detector Algorithm.....	28
IV.	Results & Analysis.....	31
4.1	Chapter Overview .....	31
4.2	Two Detector Model .....	32
4.3	Three Detector Model .....	34
4.4	Four Detector Model .....	35
4.5	Error .....	37
4.6	Analysis of the Compton Back Scatter Region.....	40
VI.	Conclusions and Recommendations for Future Study.....	44
VII.	Appendices.....	46
	Bibliography .....	70

## List of Figures

	Page
Figure 1: Regions of dominance for gamma interactions within absorbing material [1]. For the gamma photon energies and materials studied in this research, photoelectric absorption and Compton scattering are the interactions of interest.....	6
Figure 2: Photoelectric Effect process in which the photon transfers all of its energy to an atom, resulting in electron emission. [4].....	8
Figure 3: Compton scattering process in which a photon transfers a portion of its energy to an electron with the scattered photon energy. [4].....	9
Figure 4: A graphical representation of pulse height resolution.[19] .....	11
Figure 5: Diagram of typical gamma scintillation detector. The increasing number of dotted lines indicates an increase in electron population between stages of the photomultiplier. [9] .....	14
Figure 6: A typical representation of a NaI gamma spectrum resulting from a mono-energetic source. The full-energy photon peak, Compton edge, the Compton continuum, and the backscatter peak are shown.....	16
Figure 7: 3-D (left) and 2-D (right) representations of the test scene utilized for both simulated and experimental data collection. The model was divided into a $5 \times 6$ grid superimposed on the 2-D model.....	20
Figure 8: A representation of the MCNP model where boxes 2,3,4,5 are Concrete Support beams; 14, 15, 16, 18, 19 are electrical boxes. The yellow representing metal boxes (3), the green box representing column made of wood, the red square representing a graphite box, the blue box on the bottom is a room with concrete walls and the small light blue squares are concrete columns (5). Cell (1, 1) is on the bottom left, (1, 6) on the bottom right, (5, 1) upper left corner, then (5, 6) on the upper right corner.....	21
Figure 9: Relative locations of detectors (blue circles) and source (red circle) for a single simulation run. Note: Detectors and source are not to scale.....	23
Figure 10: NaI detector equipment configuration. [5] .....	24
Figure 11: Map of the experimental area with grid and counts within 662 keV photopeak per location.....	24

Figure 12: Gaussian distribution showing the standard deviation from the mean, $\mu$ , of a population .....	26
Figure 13: Example of optimal placement for 2 detectors in a simple scene. Detector A has clear LOS to grid nodes 3, 4, 8, and 9, none of which can be seen by detector B. Conversely, nodes 12, 13, 17, and 18 can only be seen by detector B; this configuration minimizes the number of nodes with clear LOS to both detectors, maximizing the probability of detection of a source placed randomly within the scene. ....	29
Figure 14: Flowchart depicting decision tree for calculating optimal detector pair placement....	30
Figure 15: Identification of grid locations using a single consecutive numbering scheme .....	31
Figure 16: A side by side representation of the 2 dimensional point attenuation kernel versus the MCNP model with 2 detectors. The results showed a strong influence to the outside corners for optimal emplacement of NaI detectors. ....	33
Figure 17: The graph above demonstrates that both models are predicting the same locations when emplacing 2 detectors.....	33
Figure 18: A side by side representation of the 2 dimensional point attenuation kernel versus the MCNP model with 3 detectors. The results showed an influence of placing the third detector in the concrete office for optimal emplacement of NaI detectors.....	35
Figure 19: The graph above demonstrates that both models are predicting the same locations when emplacing 3 detectors.....	35
Figure 20: A side by side representation of the 2 dimensional point attenuation kernel versus the MCNP model with 4 detectors.....	36
Figure 21: The graph above demonstrates that both models are predicting the same locations when emplacing 3 detectors.....	37
Figure 22: Comparison of the MCNP simulated detector responses from grid locations 18 and 24.....	39
Figure 23: Graphical representation of how particle energies were binned within MCNP.....	41
Figure 24: Detector 24 spectra from a billion particle MCNP F8 Tally .....	42
Figure 25: Detector 18 spectra from a billion particles MCNP F8 Tally .....	42
Figure 26: Detector 17 spectra from a billion particles MCNP F8 Tally .....	43

Figure 27: Graphical representation of how the solid angle calculated percentage of incident photons on the face of the object for the 2D model..... 68

Figure 28: Graphical representation of angle of incidence is assumed for the 2D model ..... 68

## **List of Tables**

Table 1: A comparison of simulated and experimental detector responses and their uncertainties .....	38
Table 2: Simulated and experimental relative uncertainties for detectors placed in grid locations 18 and 24 (Figure 15).....	39

# **OPTIMIZATION OF DETECTOR PLACEMENT FOR HIDDEN RADIATION SOURCE DETECTION**

## **I. Introduction**

### **1.1 Relevance of Work**

There is considerable interest in the development of systems which can emplace a number of detectors in order to optimize their capability to discover hidden Special Nuclear Material (SNM). While the problem sounds simple, the solution is quite complicated. Radiation signatures of shielded SNM become difficult to detect due to significant distances between detector and source locations, as well as shielding material placed between a source and the detectors. Additionally, background noise from naturally occurring radioactive materials complicates the source spectrum. Finally, variables such as time, temperature, source strength, and quantity and quality of detection equipment are factors that can make the problem much more complex.

The capability to discriminate between background and SNM radiation in a timely manner requires the correct type of detector (gamma, neutron, etc.) placed in the optimal location. This requirement dictates an accurate assessment of environmental factors; these factors, such as objects in the scene and their material composition, can be crucial in the ability to determine the presence of SNM in a particular location. The proper detector emplacement based upon environmental criteria can result in a significant increase in the probability for

isolating and securing a special nuclear material target quickly. While typically the presence of some type of nuclear radiation can be detected quickly, the determination of the exact nature of the radiation source inherently requires longer detection times in order to acquire the necessary peak photons when detecting gamma rays.

The Air Force Institute of Technology has proposed a methodology that utilizes Polarimetric Hyperspectral Images (PHSI) to improve characterization of the environment. PHSI will assist with defining the environment by determining what materials might be shielding or attenuating the source. Optimal placement of detection equipment can then be linked with the scattering or attenuating material information. By knowing the composition of materials present in the scene, optimal placement of detectors can be determined and the probability for detection can be maximized. Ultimately, this allows exploitation of the spectrum through the SNM interaction in a known environment.

The objective of this work was to investigate and develop a system for determining optimal emplacement of detectors in a known environment in order to lower detection times and increase the efficiency of detecting SNM. Additionally, the speed in which the attenuation model works could mean the difference between detecting the source or missing it.

Achievement of this objective involved the development of a model that will improve predictive capabilities for multiple radiation detectors. While we can typically find the best detector placement for one detector easily, the second detector influences the placement of the first; avoiding major overlap between detectors while simultaneously providing maximum coverage for a given scene is a non-trivial problem. The goal was to complete and experimentally validate a 2-D photon attenuation analytical transport model that would identify

the optimal location of multiple detectors to maximize the likelihood of detection and identification.

## **1.2 Hypothesis**

Fast acquisition of gamma radioisotope identification is possible without using a computationally intensive stochastic model such as the Monte Carlo n-Particle (MCNP) code. Optimization of detector placement in a given location can significantly decrease the time necessary to acquire spectra and can maximize the detection likelihood in a complex environment. This research develops this relationship utilizing 2-D point attenuation models, MCNP simulations, experimentally obtained gamma ray spectra, and a methodology that will maximize the likelihood of detection in a complex environment.

This research was comprised of three separate efforts; first, a series of simulations using an MCNP model with one gamma detector in a test environment was used to predict detector responses to a radioactive source. Second, experimental measurements were taken with a gamma detector in an analogous environment to validate the MCNP simulations. Finally, a simple 2-D photon attenuation analytical transport model was used to simulate the same analogous environment; both MCNP and analytical results were processed through an algorithm designed to predict optimal placements for multiple detectors, though likely with different confidence levels. With experimental results in good agreement with traditional MCNP simulations and subsequently comparable to the 2-D attenuation model, the use of the computationally less intensive 2-D attenuation model for detector placement was validated.



## II. Theory

### 2.1 Chapter Overview

The purpose of this chapter is to cover key topics on gamma ray interactions and detection. Additionally, previous work on gamma interactions, attenuation, detector characteristics, spectroscopy, and rules for probability and statistics will be covered. Understanding these topics is essential in designing a model that optimizes detector placement to locate and identify an unknown radiation source.

### 2.2 Gamma Radiation

Because photons have no charge or mass they can travel relatively large distances in air before interacting; this is one of the main reasons gamma signatures are important for hidden source detection. The distance that a photon will penetrate material is governed statistically by a probability of interaction per unit of distance traveled, and depends upon the photon energy and the material it is interacting with. A photon may be absorbed by an atom, scatter and change its direction of travel when interacting with an electron, or disappear and create charged particles; these processes of interactions are known as the photoelectric effect, Compton scattering and pair production. Figure 1 shows the dominant interactions for gamma interactions within an absorbing material as a function of the atomic number of the material. The focus of this work will concentrate on photoelectric and Compton scattering, as the photon energies of interest are below the pair production threshold values for most materials of concern.

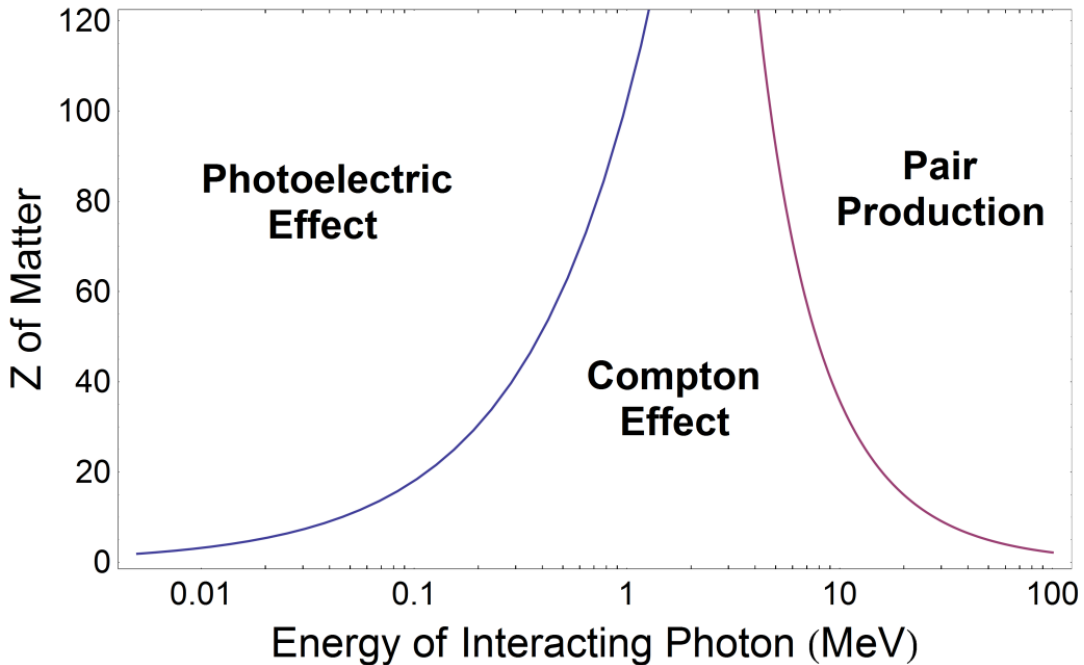


**Figure 1:** Regions of dominance for gamma interactions within absorbing material [1]. For the gamma photon energies and materials studied in this research, photoelectric absorption and Compton scattering are the interactions of interest.

### 2.2.1 Attenuation

Attenuation is the gradual loss of intensity of flux through a surface. As the thickness of the absorber gets larger there is an exponential attenuation of gamma-rays that would reach a detector. As a monoenergetic beam of photons,  $N_0$ , enters an absorbing material, some are absorbed by atoms through the photoelectric effect, undergo elastic scattering via collisions with electrons (Compton scattering), or produce particle-antiparticle pairs (pair production). The sum of these probabilities is given by  $\mu_{total}$ , the linear attenuation coefficient. The total attenuation of the photon beam can then be calculated using

$$N(x) = N_0 e^{-\frac{\mu_{total} \cdot x}{\rho}}, \quad (1)$$

where  $x$  is the distance traveled by the photon and  $\rho$  is the material density. Linear attenuation coefficients are typically listed as a function of material density. Thus, we have the mass attenuation coefficient of  $\mu_{total}/\rho$ . The attenuation coefficient  $\mu_{total}$  is a sum of the individual interaction coefficients, given by

$$\mu_{total} = \mu_{pe} + \mu_{cs} + \mu_{pp} + \mu_{rs} . \quad (2)$$

The subscripts denote the relative attenuation coefficients for the photoelectric effect ( $pe$ ), Compton scattering ( $cs$ ) and pair production ( $pp$ ), respectively. Similarly to pair production, the total contribution of Rayleigh scattering in the photon energy range examined in this work is negligible and will be ignored.

Gamma-ray photons are also characterized by their mean free path,  $\lambda$ , which is simply the inverse of the linear attenuation coefficient.

$$\frac{1}{\mu_{total}} = \lambda \quad (3)$$

### 2.2.1.1 Photoelectric Effect

The photoelectric effect is the ejection of electrons from an atom or molecule as a result of light absorption. The probability of producing a photoelectron when light interacts with an atom is strongly dependent on the photon energy and the atomic number of the interaction medium. In general, the probability (cross section) is maximized for low energy photons, having energies less than a few hundred keV. Additionally, for a fixed photon energy, the probability of interaction increases with increasing atomic number,  $Z$ , of the absorber material (fig.1). A

graphical representation of the photoelectric effect is shown in Figure 2. The energy of the ejected electron is

$$E_e = E_p - E_b , \quad (4)$$

where  $E_p$  is the incident photon energy and  $E_b$  is the electron binding energy.

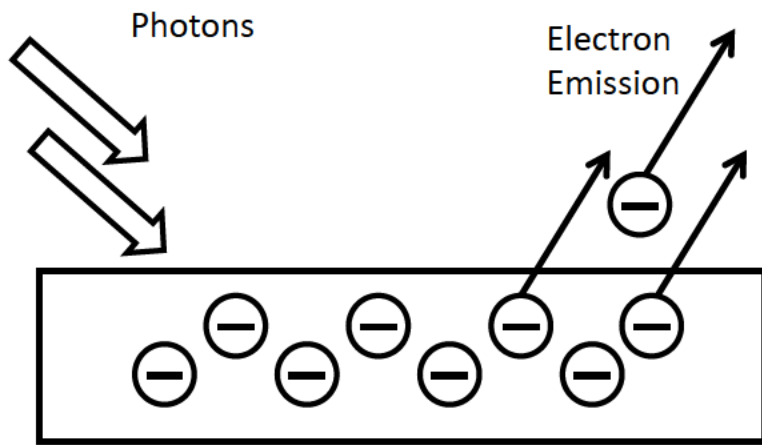


**Figure 2: Photoelectric effect process in which the photon transfers all of its energy to an atom, resulting in electron emission. [4]**

#### 2.2.1.2 Compton Scattering

Compton scattering entails a photon transferring only part of its energy to an electron, with the photon leaving the collision site on a different trajectory with lower energy. This process is displayed graphically in Figure 3. Note that the figure is in two dimensions, and in three dimensions there will be an azimuthal scattering angle ( $\phi$ ).

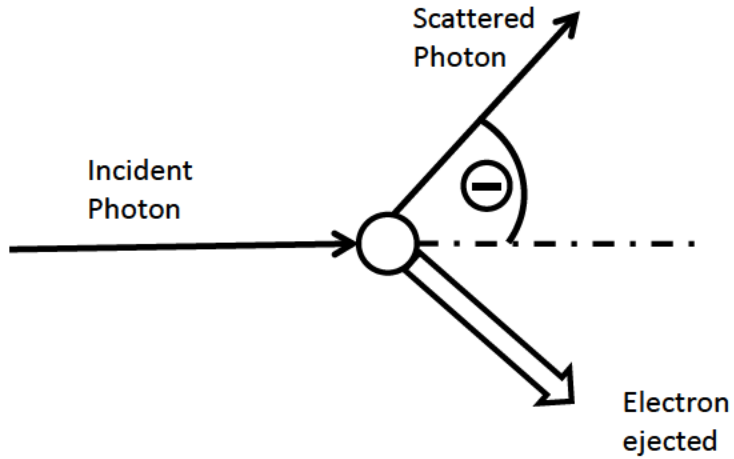


**Figure 3:** Compton scattering process in which a photon transfers a portion of its energy to an electron with the scattered photon energy. [4]

Conservation of momentum and energy enables the calculation of the shift in wavelength of scattered photon. A photon of energy  $h\nu$  and momentum  $h\nu/c$  is incident on a stationary, free electron of energy  $m_ec^2$ . After the collision, the photon is scattered at an angle  $\theta$  with energy  $h\nu'$  and momentum  $h\nu'/c$ . The electron then recoils at an angle  $\phi$  with total energy  $E'$  and momentum  $P'$ . Conservation of total energy gives

$$h\nu + m_ec^2 = h\nu' + E' \quad (5)$$

Conserving momentum in the horizontal and vertical directions yields

$$\frac{h\nu}{c} = \frac{h\nu'}{c} \cos \theta + P' \cos \phi, \text{ and} \quad (6)$$

$$\frac{h\nu'}{c} \sin \theta = P' \sin \phi \quad (7)$$

By eliminating  $P'$  and  $\phi$  from these equations and solving for the energy of the scattered photon  $h\nu'$  yields

$$h\nu' = \frac{h\nu}{1 + (h\nu/m_e c^2)(1 - \cos \theta)} \quad (8)$$

Utilizing the relationship  $\lambda = c/v$ ,  $\Delta\lambda$  is determined to be

$$\Delta\lambda = \lambda' - \lambda = \frac{h}{mc}(1 - \cos \theta) \quad (9)$$

Note that the shift in wavelength is only dependent upon the angle  $\theta$  and not the incident photon frequency. For an incident photon with a given energy, the angular distribution of the scattered photon is described by the Klein-Nishina formula, given by

$$\frac{d\sigma}{d\Omega} = \frac{r_e^2}{2} \frac{1}{[1 + \gamma(1 - \cos(\theta))]^2} \left[ 1 + \cos^2(\theta) + \frac{\gamma^2(1 - \cos(\theta))^2}{1 + \gamma(1 - \cos(\theta))} \right] \quad (10)$$

where  $r_e^2 = 2.92 \cdot 10^{-15} m$ ,  $\gamma = \frac{E_0}{m_e c^2}$ , and  $\theta$  is the photon scattering angle in the range  $0 \leq \theta \leq 180$

degrees.

## 2.3 Gamma Detection

### 2.3.1 Detector Characteristics

An important metric for radiation detectors is energy resolution; this characteristic is a measure of the detector's ability to distinguish between incident photons of similar energies. The full width at half maximum (FWHM) of a photon peak is a method of verifying a detector's

resolution. The FWHM can be measured directly from the detector using a mono-energetic gamma source, then the detector's resolution  $R_{\text{exp}}$  is determined using

$$R_{\text{exp}} = \frac{FWHM}{H_0} \quad (11)$$

where the value  $H_0$  is the amplitude of the full energy peak (FEP). A graphical representation of pulse height resolution is shown in Figure 4.

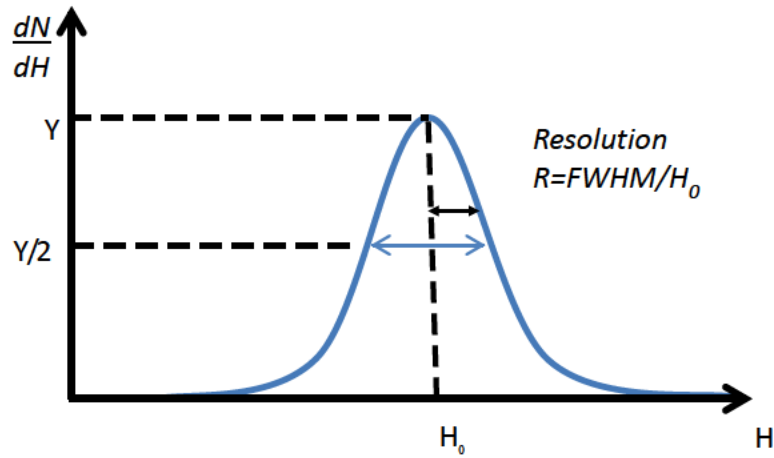


Figure 4: A graphical representation of pulse height resolution. [19]

In addition to the experimental method and assuming a Gaussian distribution, the FWHM can be calculated if the standard deviation is known by

$$FWHM = \sqrt{2 \times \ln(2)} \times \sigma \approx 2.35\sigma \quad (12)$$

where  $\sigma$  is the standard deviation.

Finally, the theoretical limit to resolution can be demonstrated through the proportionality of the square root of the photon energy with the FWHM of that peak.

$$\ln(R) = \ln(K) - \frac{1}{2}\ln(E) \quad (13)$$

where  $R$  is the resolution of a peak,  $E$  is the energy of that peak, and  $K$  is a constant particular to a specific scintillation-photomultiplier tube combination. This provides a relation between resolution and energy so that a plot of  $\ln(R)$  versus  $\ln(E)$  will yield a linear relationship with a slope of  $-1/2$ . [6] Experimental data can be validated against this theoretical limit to determine if and to what degree other sources of peak broadening are present.

Two other important areas of interest in terms of gamma detectors are their absolute and intrinsic efficiencies. The absolute efficiency is a measure of the overall ability of the detector to detect radiation from the given source. It takes into consideration the detector properties and geometry of the scenario to include the distance of the detector from the source. The equation used to calculate absolute efficiency is [9]

$$\epsilon_{\text{abs}} = \frac{\text{no.pulses recorded}}{\text{no.quanta emitted by source}} = \frac{N_{\text{rec}}}{S_a} \quad (14)$$

The intrinsic efficiency is a measure of how effective a detector is at measuring radiation that passes through the detection chamber. The intrinsic efficiency,  $\epsilon_{\text{int}}$ , can be calculated based on the output of the detector and theoretical calculations of incident radiation [9].

$$\epsilon_{\text{int}} = \frac{\text{no. of pulses recorded}}{\text{no. of radiation quanta incident on detector}} \quad (15)$$

To calculate the intrinsic efficiency from the absolute efficiency the solid angle of the radiation from the perspective of the detector is required and can be calculated with Equation (18). The calculation of the solid angle relies on the distance of the source from the detector

window,  $d$ , and the radius of the window,  $a$ . The number of radiation quanta at the detector window is subsequently determined using the source activity,  $S_a$ , which is determined from the isotope data.

$$\Omega = 2\pi \left( 1 - \frac{d}{\sqrt{d^2 - a^2}} \right) \quad (16)$$

It is more convenient to use and tabulate the values of the intrinsic efficiency due to the lower reliance on geometry. The intrinsic efficiency and absolute efficiency are related by Equation (19). Generally the intrinsic efficiency depends primarily on the detector material, radiation energy, physical thickness of the detector, and the direction of the incident radiation. The intrinsic efficiency still does rely on geometry, but due to the path length of the radiation through the detector in relation to the detector-source distance, the effect is minimized [9]. The  $4\pi$  divergence accounts for isotropic emission of radiation by the source.

$$\epsilon_{abs} = \frac{\Omega}{4\pi} \epsilon_{int} \quad (17)$$

### 2.3.2 Types of Detectors

#### 2.3.2.1 Scintillators

Scintillation detectors rely on the reaction of ionizing radiation with certain materials to produce optical photons; these are produced through fluorescence, or for the purposes of this experiment prompt fluorescence, which is the prompt emission of visible radiation from a material following excitation, in this case ionizing radiation excitation. The best scintillation materials

have a high absorption rate and emit the majority of their light in the form of fluorescence. These are one of the oldest techniques for detecting ionizing radiation and is still an effective and efficient means of detecting ionizing radiation today. The scintillation detectors vary, based on their materials and light sensors, but most modern scintillators rely on photomultiplier tubes and photodiodes to convert light into an electrical pulse that can be measured and analyzed through spectroscopy. An example of a typical gamma detector coupled to a photomultiplier is shown in Figure 5.

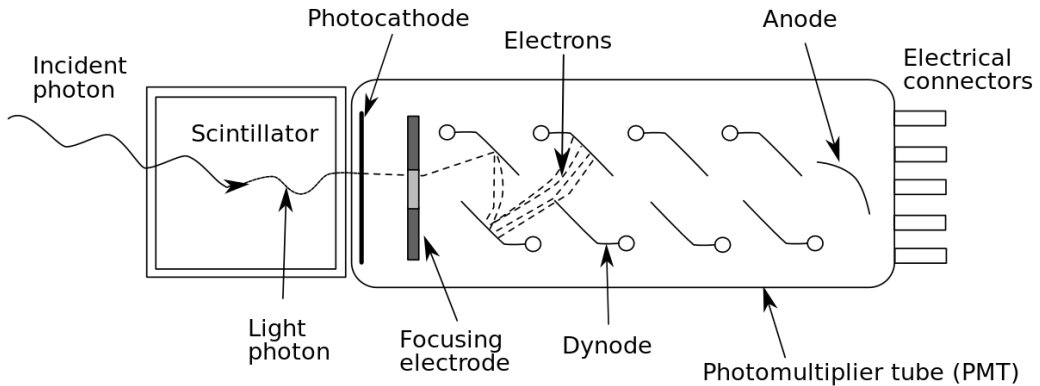


**Figure 5: Diagram of typical gamma scintillation detector. The increasing number of dotted lines indicates an increase in electron population between stages of the photomultiplier. [9]**

Inorganic scintillation detectors, such as the NaI(Tl) used in this work, generally have a high light output and linear responses over a wide energy range, but generally have relatively slow response times. Organic scintillators, on the other hand, generally have faster response times but produce less light. Also of note is that high Z materials and high density of inorganic crystals make scintillation detectors more effective for the gamma-ray spectroscopy, which is the focus of this work. [9]

### 2.3.2.2 Semiconductor Detectors

Semiconductor detectors measure radiation by means of the number of charge carriers set free by radiation interacting in the detector active volume, which is arranged between two electrodes. Ionizing radiation produces free electrons and holes. The number of electron-hole pairs depends on the energy deposited by the radiation to the semiconductor active region. Under the influence of an electric field, electrons as well as holes travel to the electrodes, where they give rise to a current pulse that can be measured.

## 2.4 Gamma Spectroscopy

Spectral peaks are traditionally used to identify a gamma-emitting radioactive source. In the case of a mono-energetic photon source, the full-energy peak represents the pulses that arise from the full energy deposition in a short enough time to be considered a single event in the detection medium. Additional peaks arise from partial energy deposition from Compton scattering and pair production where some of the energy of the photon interaction escapes the detector volume. For each peak the centroid represents the photon energy  $E_0$ , and its net area above background represents the total number of full-energy interactions in the detector and is usually proportional to the activity, source-detector distance, and solid angle subtended by the emitting isotope. Its width is determined primarily by the statistical fluctuations in the charge produced from the interactions plus a contribution from the pulse-processing electronics. If the characteristic gamma peaks are well resolved, there is little need to evaluate the Compton continuum spectra for source identification [7]. However, if the gamma peaks are not easily identifiable, additional information can be gained from the Compton continuum. A typical spectrum is shown below in Figure 6, with the photopeak on the far right.

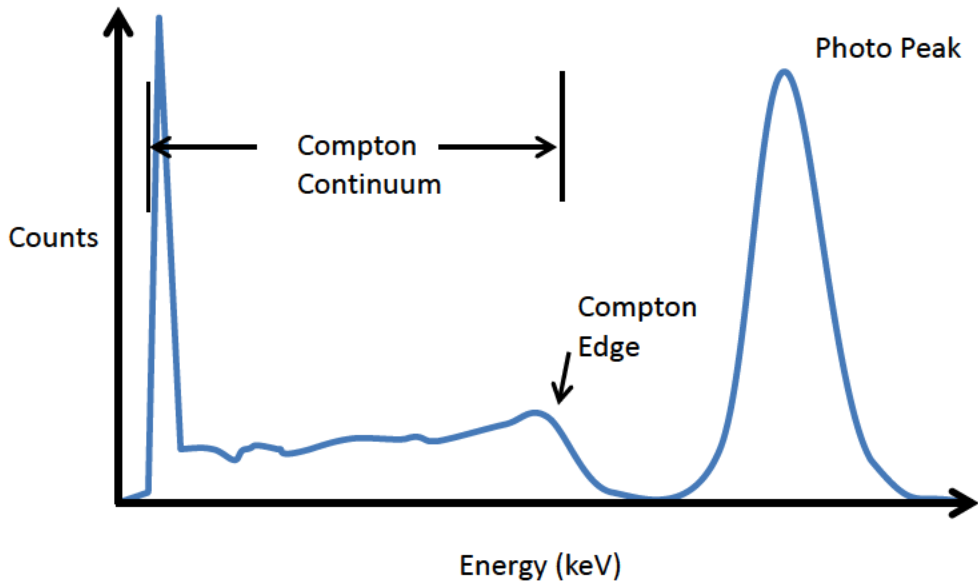


**Figure 6:** A typical representation of a NaI gamma spectrum resulting from a mono-energetic source. The full-energy photon peak, Compton edge, the Compton continuum, and the backscatter peak are shown.

#### 2.4.1 The Compton Edge and the Compton Continuum

As discussed earlier in the description of Compton scattering, the gamma ray is not absorbed, but rather scattered through an angle  $\theta$  by an electron, which recoils and carries away some of the gamma ray's energy  $E$ . The scattered gamma ray can then potentially escape from the scintillator. The probability that a Compton scattered gamma ray scatters again in a typical size scintillator such as a 3×3 inch NaI(Tl) is quite small (1% to 10%), which means it is unlikely to detect a gamma ray that has undergone two Compton scatterings. The gamma ray initial wavelength is

$$\lambda = \frac{hc}{E} = \frac{1240 \text{ nm}}{E} \quad (18)$$

where  $E$  is in eV. The change in wavelength is

$$\Delta\lambda = \frac{h}{mc}(1 - \cos\theta) = 0.00243(1 - \cos\theta)nm \quad (19)$$

where  $h$  is Planck's constant,  $m$  is the mass of the electron and  $c$  is the speed of light. From this equation the energy loss of the gamma ray will vary from zero (when  $\theta = 0^\circ$ ) to a maximum corresponding to a wavelength shift of 0.00486 nm (when  $\theta = 180^\circ$ ). This maximum energy loss is called the Compton edge. The energy distribution of Compton scattered electrons is essentially a constant. So the Compton spectrum produced by a photomultiplier tube is an almost flat plateau from zero energy up to the Compton edge where it drops off sharply (at a rate limited by the energy resolution of the tube). The Compton edge is calculated by

$$E_C = h\nu - h\nu|_{\theta=180} = h\nu - \frac{h\nu}{1 + 2h\nu/m_0c^2} \quad (20)$$

If the Compton edge is known, then the energy of the source photons can be calculated [7].

#### 2.4.2 Backscatter Peak

The backscatter peak is caused by gamma rays that have interacted by Compton scattering in one of the materials surrounding the detector. The theoretical energy of the backscatter peak is given by

$$h\nu'|_{\theta=180} = \frac{h\nu}{1 + 2h\nu/m_0c^2} \quad (21)$$

Gamma rays scattered by more than  $110^\circ$  -  $120^\circ$  will emerge with nearly identical energies in the 200- to 250-keV range. Therefore, a mono-energetic source will give rise to many scattered gamma rays whose energies are very close in value and result in a peak observed in the recorded spectrum [9].

#### 2.4.3 Background and Minimum Detectable Activity

Because background radiation is always present in any physical scenario, a method must be established for separating out the background from the source that result in the detectable signal. This criterion is established as a minimum detectable activity, MDA. MDA is the minimum amount of radioactive material necessary to yield detection. This detection limit can be written as

$$Limit = t \times MDA \times \gamma \times G \times \varepsilon_i \times \varepsilon_f, \quad (22)$$

where *MDA* is the minimum detectable activity, *t* is the measurement time,  $\gamma$  is the gamma-ray yield per disintegration, *G* is the geometric factor,  $\varepsilon_i$  is the detector intrinsic efficiency, and  $\varepsilon_f$  is the fraction of interactions which are summed in the algorithm (i.e. the photopeak in this experiment).

Note, that detector intrinsic efficiency is a strong function of distance to the source and of energy. So the MDA can only be properly defined under limited conditions. Instead, the energy of the source, the distance to the source, and the background radiation level required to compare the models must be known [13].

### III. Methodology

#### 3.1 Chapter Overview

The purpose of this chapter is to explain the processes that were used to validate the multi-detector algorithm. First, a single detector MCNP model was verified against experimental measurements from a test scene. Next, a validation of the 2-D attenuation model against the MCNP model was conducted so all three results could be utilized and cross-referenced to compare to the optimal detector model. Then, an execution of the multi-detector algorithm, utilizing the 2-D attenuation model, was executed and compared to a multi-detector model utilizing the 3-D simulation output from MCNP. Finally, a MCNP tally was developed in order to display the optimal multi-detector algorithm model.

#### 3.2 MCNP

In this research, MCNP was used to simulate a test scene in order to gain insight into how multiple detectors might be optimally placed when searching for lost or hidden sources. The simulated environment was based on a real location; measurements of the scene were taken using a laser rangefinder and the composition of various materials present was estimated. Additionally, the scene was divided in the x-y plane into a rectangular  $5 \times 6$  grid, with each node measuring  $1 \times 2$  meters. The behavior of multiple detectors, one at the center of each node, was then simulated using a single mono-energetic gamma source.

MCNP is a Monte Carlo particle transport code that was developed by Los Alamos National Laboratory. The simulation program tracks the random walk of radioactive particles as they interact in materials of a known environment. The program has the ability to predict the

radiation flux at a particular location emitted by a given radiation source. The Monte Carlo code can also be utilized to predict the response of a detector in a radiation field. The program is used throughout the nuclear community for research, specifically in the areas of reactor design, detector design, and accelerators. For this research, a F4 tally was used to estimate the flux of photons at 662 keV.. The F4 tally, called a volume averaged path-length tally, simulates a known source, which was placed at various locations in the simulated basement. The simulation placed a detector in 29 of the 30 grid locations and the source in the leftover grid. The simulation was executed 30 times in order to get the flux of all the cells with the source in all 30 locations. The layout of the MCNP model of the area utilized in the research is shown in Figure 7.

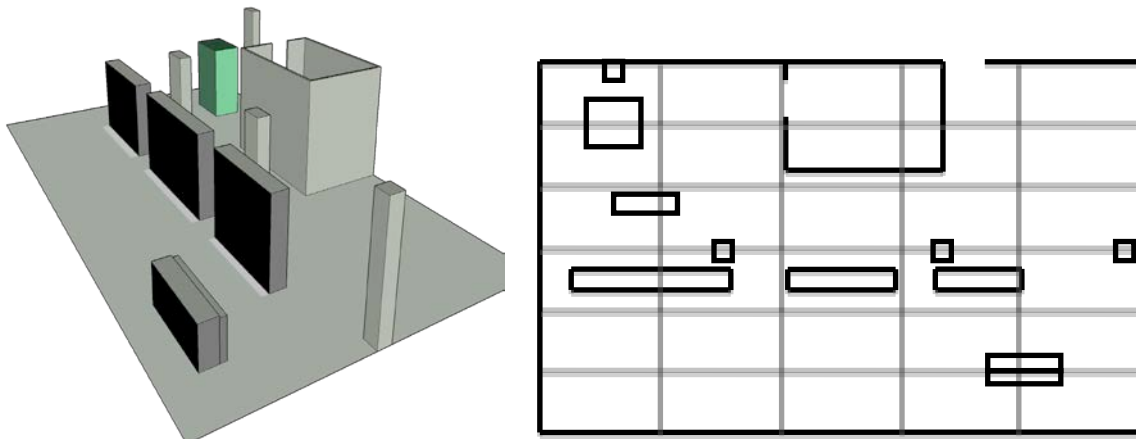
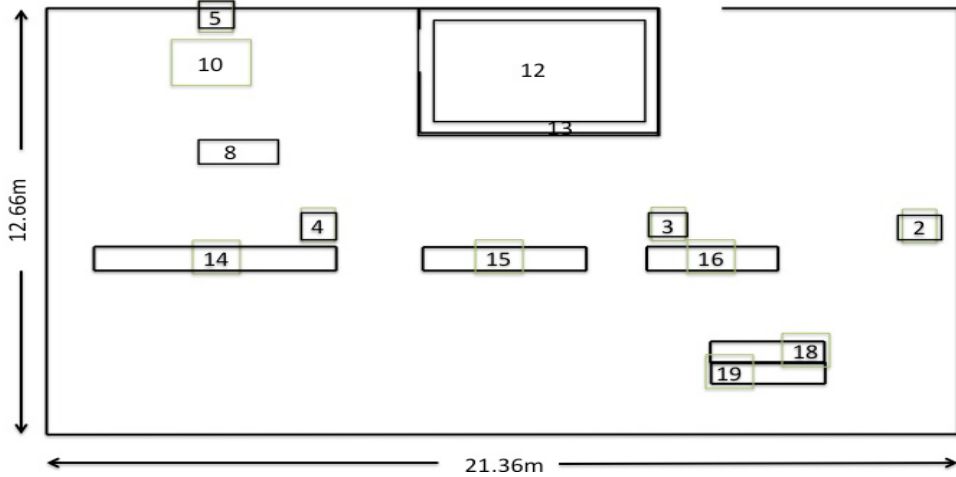


Figure 7: 3-D (left) and 2-D (right) representations of the test scene utilized for both simulated and experimental data collection. The model was divided into a  $5 \times 6$  grid superimposed on the 2-D model. Dark grey represents steel, and the lighter grey represents concrete.

An example of how the MCNP input was developed is shown in Figure 8. The importance of defining all materials as accurately as possible is essential to model validation.



**Figure 8: A representation of the MCNP model where boxes 2,3,4,5 are Concrete Support beams; 14, 15, 16, 18, 19 are electrical boxes.**

### 3.2.1 MCNP Tally

The F4 tally was used to calculate the average flux on each cell. It is explained by supposing a particle of weight  $W$ , and energy  $E$  makes a track length within a specified volume. The segment makes a contribution to the flux in the cell, where  $T$  is the track length. The sum of these contributions is displayed in the F4 tally from MCNP. This tally can be represented as

$$F4 = \frac{1}{V} \int_V dV \int_E dE \int_{4\pi} d\Omega \Phi(r, E, \Omega), \quad (23)$$

where  $E$  signifies the energy and  $\Phi$  the angular distribution of the fluence as a function of the position. The sum of all the contributions will be reported as the F4 tally results after running the simulation. This is an estimate of the number of particle-track lengths per unit volume.

### 3.2.2 Simulation Setup

MCNP is very useful for predicting detector response, but cannot completely replicate the photon interactions for a given detection problem. The experimental configurations are often vastly more complex and with many more variables than can be modeled in a simulation; as a consequence, simulation results never completely match those obtained experimentally (Figure 4). A way to ensure that similar data are being compared is to simulate the data until the relative errors are of similar values. For example, if the relative error in experimental data is 5% for the 100 keV energy bin (for a given source-detector geometry) then the simulation must run enough particles so that after solid angle adjustments, background count subtraction, and energy binning, a 5% relative error is also achieved in the 100 keV energy bin [7].

With the MCNP model built to match the experimental scene, shown in Figure 7, a series of simulations were run; a  $^{137}\text{Cs}$  source was placed in the center of a grid node and detector responses were recorded at the centers of all other nodes. This was repeated, with the source placed in the center of each of the 30 nodes, and data collected for detectors in the other 29. The simulated detector counts are displayed in Appendix A.

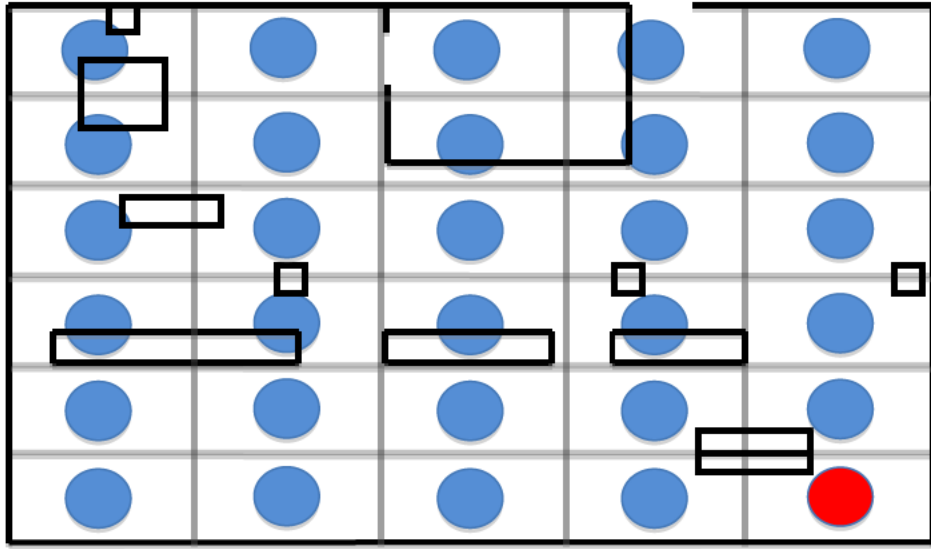


**Figure 9: Relative locations of detectors (blue circles) and source (red circle) for a single simulation run.**  
**Note: Detectors and source are not to scale.**

### 3.3 Experimental Setup

Two test sources,  $^{137}\text{Cs}$  and  $^{60}\text{Co}$  were used to calibrate the equipment and compare the backgrounds. The detector, a  $3 \times 3$  NaI, was placed on a moveable cart and oriented vertically to the surface of the cart to provide omnidirectional detection capability. This was done to ensure consistent measurements regardless of the source position relative to the detector. The source was placed on a wood pedestal at the same height as the detector position chosen in order to minimize errors in measurement and subsequent calculations.

After setting up the equipment in the configuration shown in Figure 10, a calibration file was created utilizing the Ortec GammaVision software to ensure correct measurement of the background noise. This calibration file can be used as a baseline for future data collection.

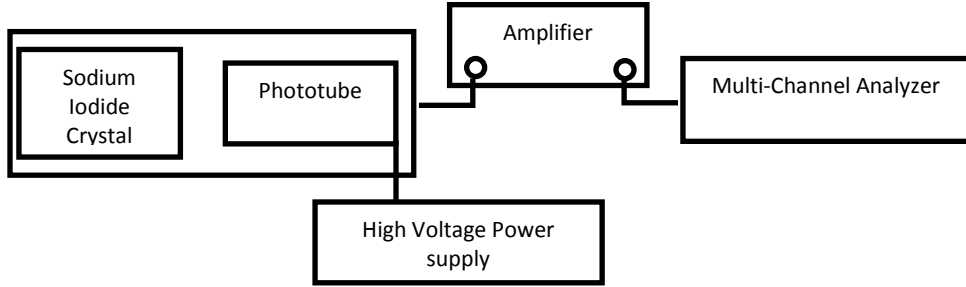


**Figure 10: NaI detector equipment configuration. [5]**

### 3.3.1 Data Collection

A  $5 \times 6$  grid of the experimental scene, the same as was used in MCNP simulations, was created and the area was marked off in equal rectangles as shown in Figure 9. The source was placed in location 6-1 and the spectrum was measured at the other 29 grid locations.

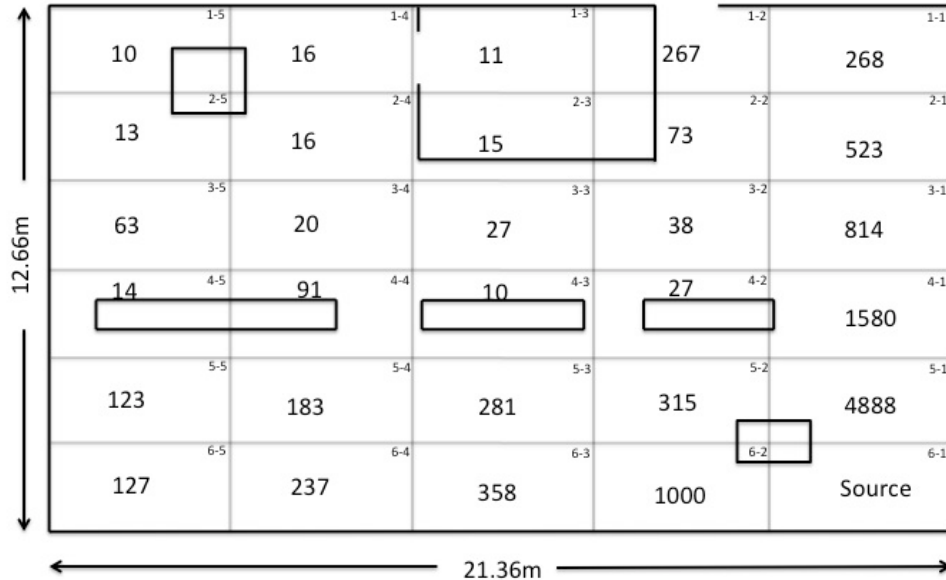


**Figure 11: Map of the experimental area with grid and counts within 662 keV photopeak per location.**

Each spectrum was saved to a file corresponding to the grid location where the detector was placed. The total counts in the area of interest (i.e. the 662 keV photopeak) were extracted

from the spectra; the counts for all grid locations are displayed graphically in Figure 11. This data was compared against the MCNP results in order to validate the simulated detector behavior.

### 3.4 Statistics

Detectors in general must rely on a limited number of events to provide meaningful information in a short amount of time. Statistical models are an important means of analyzing the information a detector records. Distribution models such as Poisson provide good analysis of moderate sets of data over 20 counts, while Gaussian models are useful for modeling random probability distributions.

Experimental data is analyzed using the experimental mean,  $\bar{x}_e$ , experimental standard deviation,  $s$ , and the experimental variance,  $s^2$ . These experimental measurements are comparable to the theoretically calculated properties of mean,  $\mu$ , standard deviation,  $\sigma$ , and variance,  $\sigma^2$ . Equations 3.2 and 3.3 show how the experimental mean and variance are calculated. Standard deviation is simply the square root of the variance.

$$\bar{x}_e = \frac{1}{N} \sum_{i=1}^N x_i \quad (24)$$

$$s^2 = \frac{1}{N-1} \sum_{i=1}^N (x_i - \bar{x}_e)^2 \quad (25)$$

Using the standard deviation can be an important way to analyze the quality of experimental data. Using the statistical model of a Gaussian distribution we can measure the goodness of fit of the data. The area within one standard deviation, which is  $\bar{x}_e - \sigma < \bar{x}_i < \bar{x}_e + \sigma$ , should include approximately 68% of the experimental values. Applying the same relationship

to  $2\sigma$  and  $3\sigma$  will result in approximately 95% and 99.7% of expected values to be within that range. Figure 12 is a good graphical representation of this relationship. The values in Figure 12 show the expected value in single iterations of  $\sigma$  requiring the addition of the amounts to get the expected total percentage of values within a given  $\sigma$  range. While Figure 12 uses the  $\mu$  as the center of the normal distribution the  $\bar{x}_e$  is used when trying to apply the model to experimental results.

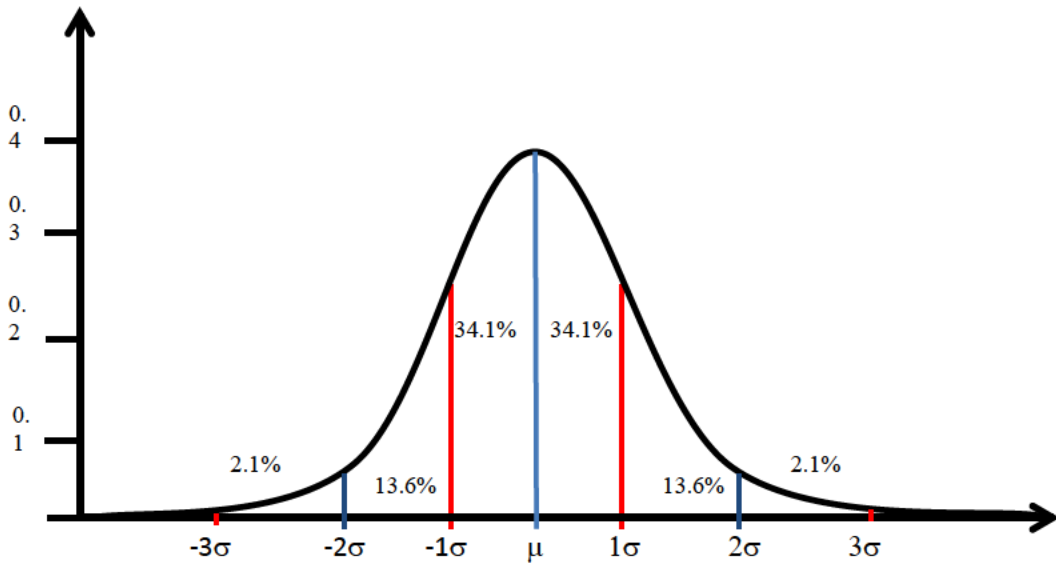


**Figure 12: Gaussian distribution showing the standard deviation from the mean,  $\mu$ , of a population.**

When the data fits Poisson or Gaussian models, we are able to use a standard deviation approximation  $s \approx \sqrt{x_i} \cong \sigma_i = \bar{x}_e$ . With the same data we are able to apply a  $3\sigma$  test, which allows us to estimate to a 99.5% confidence what we would expect measurements,  $x_i$ , to fall. Measurements outside of this range are considered outliers and are rejected.

$$\bar{x}_e - 3\sigma < x_i < \bar{x}_e + 3\sigma \quad (26)$$

The frequency distribution is calculated in Equation (29) and is useful when comparing the distribution of the experimental data to a Poisson or Gaussian distribution. For comparison the equations for calculating a Poisson and Gaussian distribution are given in Equation (30) and (31), respectively.

$$F(x) = \frac{\text{Number of occurrences of value } x}{N} \quad (27)$$

$$P_1(x) = \frac{\left(\bar{x}_e\right)^x e^{-\bar{x}_e}}{x!} \quad (28)$$

$$P_2(x) = \frac{1}{\sqrt{2\pi\bar{x}_e}} e^{\left(\frac{-(x-\bar{x}_e)^2}{\bar{x}_e}\right)} \quad (29)$$

### 3.5 Analytical model in 2-D

A cross section of the 3-D MCNP geometry, shown in Figure 7, was used as the basis for a basic 2-D attenuation model. The attenuation of a gamma source from one grid node to another node was calculated using a simple ray-tracing approach; a straight line was drawn between each detector and source position, and path lengths through any intervening objects were calculated.

Total attenuation of the source by the objects crossed was found with

$$I = I_0 \prod_i e^{-\mu_i x_i} \quad (30)$$

where  $I$  is the reduced intensity of the source,  $I_0$  the original intensity, while  $\mu_i$  and  $x_i$  are the attenuation coefficient and thickness of the  $i^{\text{th}}$  material between the source and detector, respectively. An example case would be the detector located in cell (2, 5) and the source in cell

(6, 1); the radiation will be attenuated by air, concrete, and wood, such that the exponent in Equation (32) becomes

$$e^{-\mu_{air}x_{air}} \cdot e^{-\mu_{conc}x_{conc}} \cdot e^{-\mu_{wood}x_{wood}} \quad (31)$$

Finally, geometric attenuation was taken into account by Equation (18), assuming that the detector is a right circular cylinder. As with the MCNP model described previously, these calculations were performed for every possible source-detector combinations, resulting in a three dimensional matrix of predicted detector responses as a function of source location.

### 3.6 Multi Detector Algorithm

For a given source location in a scene divided into  $n$  grid nodes, there are

$$\frac{(n-1)!}{r!((n-1)-r)!} \quad (32)$$

combinations for the placement of  $r$  detectors. If the source location is not known *a priori*, the optimal detector placements have the shortest, most uninterrupted lines of sight (LOS) to the remaining grid locations. For a single detector, this placement is simple to determine; multiple detectors impose a further constraint in that the overlap in their fields of view (FOV) must be minimal to maximize detection probability. A simplified example of this is shown in Figure 13.

1	2	3	4	 5
6		 7 8	9	10
11	12	13	14	15
 16	17	18	19	20

**Figure 13: Example of optimal placement for 2 detectors in a simple scene. Detector A has clear LOS to grid nodes 3, 4, 8, and 9, none of which can be seen by detector B. Conversely, nodes 12, 13, 17, and 18 can only be seen by detector B; this configuration minimizes the number of nodes with clear LOS to both detectors, maximizing the probability of detection of a source placed randomly within the scene.**

For a more complicated scene, such as the one shown in Figure 7, there are 406 combinations for placing two detectors; calculating all possible LOS for each grid node is not difficult, but does not take into account that gamma photons of sufficient energy can penetrate through objects in the scene. This is rectified by substituting predicted detector response for LOS as the metric used in our calculations. A source is placed in a single node and the predicted responses of all possible detector pair combinations are compared; if the difference in responses between a pair of detectors is greater than some arbitrary value, we can consider that pair sufficiently separated to minimize overlap and assign a value of 1. If the difference is less than the value, a 0 is assigned; this results in a  $n \times n$  square matrix of ones and zeros. By repeating the procedure for every source location and tallying the assigned values for each detector pair, the optimal combinations are determined to be those with the highest score. A flowchart representation of this process is shown in Figure 14.

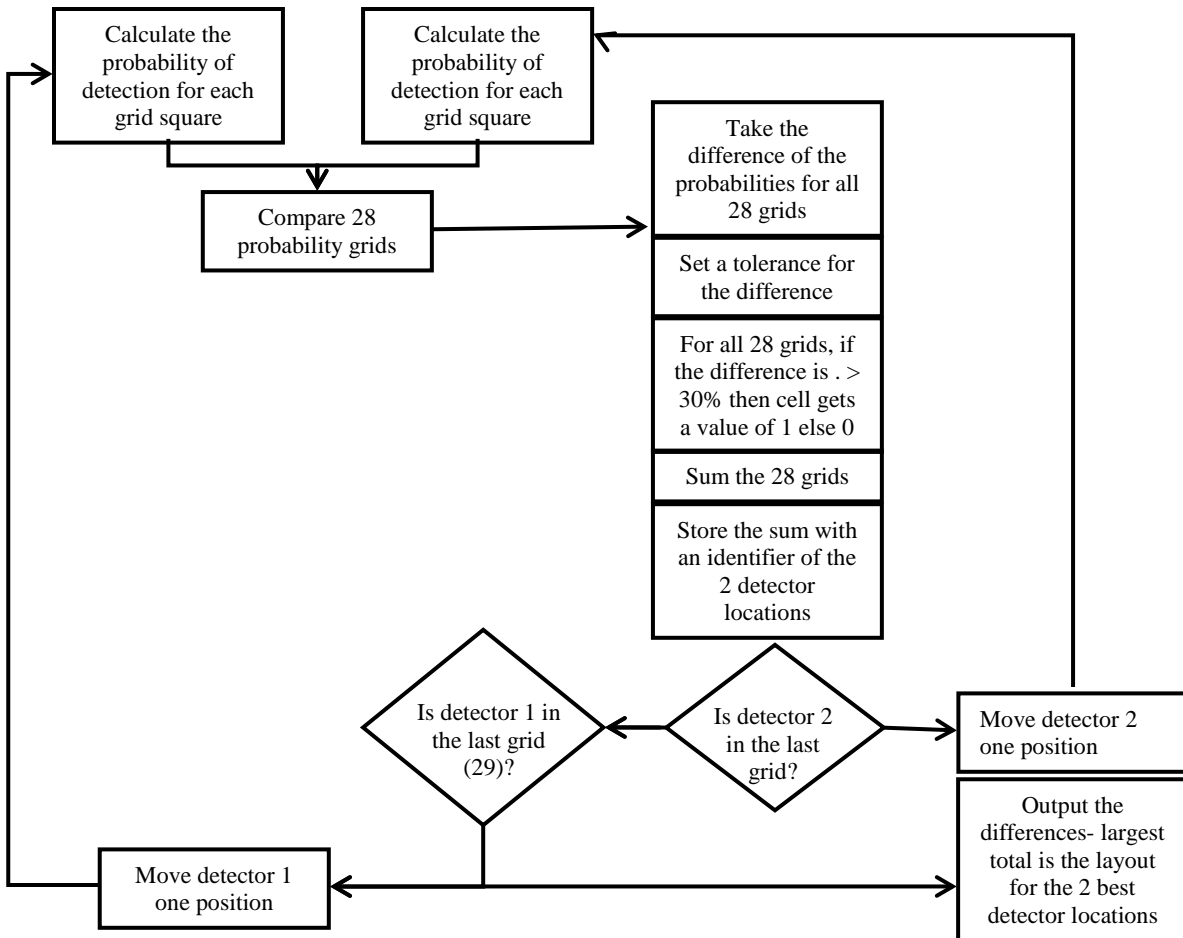


**Figure 14: Flowchart depicting decision tree for calculating optimal detector pair placement.**

This algorithm was used to process the 2-D analytical model and MCNP simulation outputs; first for two detectors, then extended up to the placement of 5 detectors. Comparisons of the algorithm results are presented in chapter IV.

## IV. Results & Analysis

### 4.1 Chapter Overview

The purpose of this chapter is to describe the results of applying the methodology previously explained in Chapter 3. First, a comparison of the optimal 2 detector model to the experimental measurements will be presented and then the results from using the 4 detector model will be discussed. Additionally, the results from the application of the MCNP Compton backscatter model will be described. The results will ultimately show that optimal detector locations determined using the 2-D attenuation model compare favorably to those selected using the MCNP model. For simplification purposes, the grid numbering scheme shown in Figure 15 will be used in the following analysis.

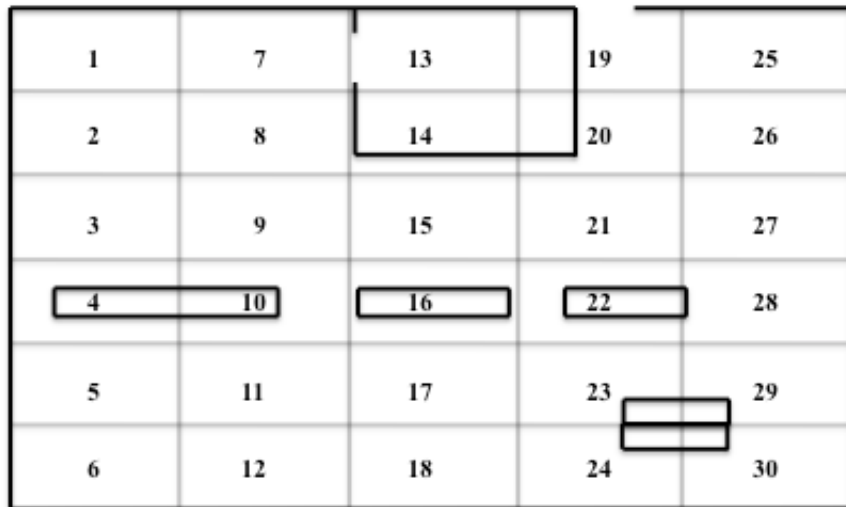
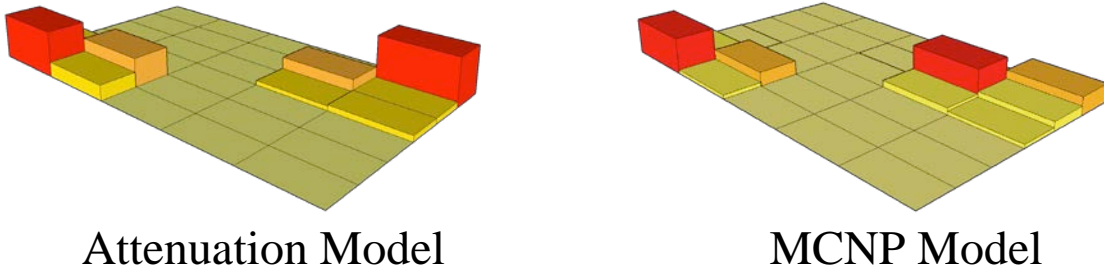


Figure 15: Identification of grid locations using a single consecutive numbering scheme

## 4.2 Two Detector Model

The algorithm from Chapter 3, Figure 14, was used to determine the optimal detector locations for two 3x3 NaI detectors. The algorithm compares the probability of detecting a source from various detector locations and produces an optimal placement of two detectors when the location of the source is unknown. The optimal placement of the two detectors, as determined by this algorithm using the 2-D attenuation model for detection probability, is detectors in position 6 and position 25. This result is displayed graphically on the left side of Figure 16. The number of grids outside of tolerance for this location was 25. Ultimately this means that the difference between the probabilities of detection was greater than the tolerance of 30 percent in 25 different grid locations for the detector placements of position 6 and position 25. The outside corners are determined to be the best locations because they have the highest detection probability for the most number of grid locations, when they act as a set of two detectors. The algorithm was then implemented using the detection probabilities produced by MCNP; the results showed that the optimal detector locations were 6 and 20, with the number of grids outside the tolerance totaling 22.

The algorithm is designed to determine where the best combination of 2 detectors should be located. However, determining the second and third best locations is significantly more difficult. An example of this problem is determining the second best location. Detector locations 6 and 25 are consistently paired with other grid squares to produce similar values (i.e. the pair 6-20 has the same value as 11-25). The results of analyzing the top 30 pairs of detector locations using the algorithm are shown in Figure 17, which displays the number of times a certain grid is displayed in an optimal pair.



**Figure 16:** A side by side representation of the 2-Dattenuation model versus the MCNP model with 2 detectors. The results showed a strong tendency for optimal detector locations in the outside corners for optimal emplacement of NaI detectors.

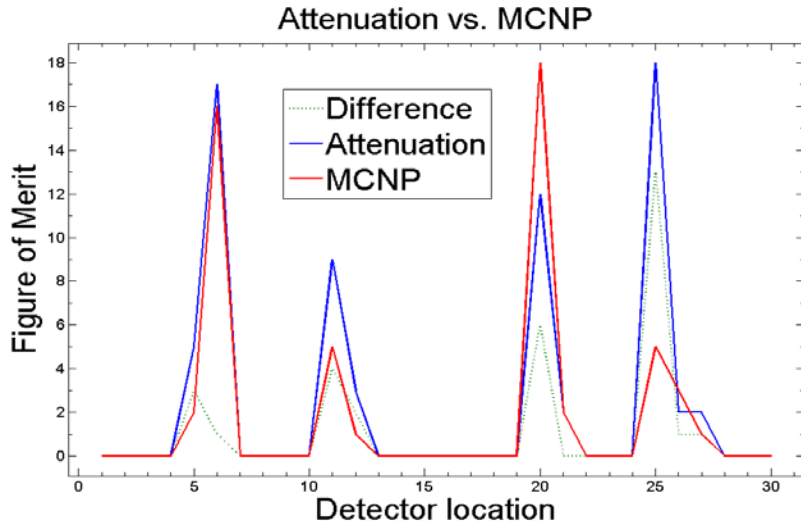


**Figure 17:** Frequency of occurrence of the optimal locations for the two detectors for the top 30 pairs of detector locations from the algorithm for both the 2-D attenuation and MCNP models. The difference between the algorithm results when using each model is also shown.

### 4.3 Three Detector Model

The initial algorithm was utilized and then expanded by adding an additional outside loop for the third detector. The computational time increases with the addition due to the significant number of additional calculations required. Both models placed the third detector in the concrete enclosure (grid locations 13 and 14 in Figure 15). This is an expected outcome due to the fact that it has the lowest probability of detection from the locations chosen in the two detector model.

The 2-D attenuation model produced optimal locations of 5-13-26, differing very little from the MCNP model optimal detector placements of 4-14-27. Additionally, the tolerance had to be lowered to produce significant difference in detector locations. This is expected, with a third detector since, there is significant overlap of detector capability as more detectors are added into a relatively small space. As to the specific locations of the detectors, the MCNP model pushed the two detectors which were placed in the outside corners in the two detector algorithm to the middle of the outside wall, as shown in Figure 18 and Figure 19. This indicates MCNP is utilizing a material for the concrete wall that attenuates the photons less than the analytical model. Of note, the tolerance needed to be lowered to gain refinement due to overlap, and the strength of the figure of merit decreased due to this overlapping of detectors.

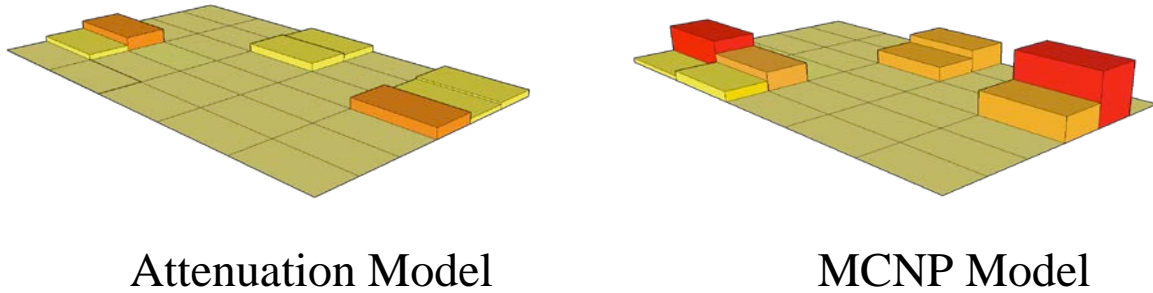


**Figure 18:** A side by side representation of the 2-D attenuation model versus the MCNP model with 3 detectors. The results displayed placing the third detector in the concrete office for optimal emplacement of the third NaI detector.

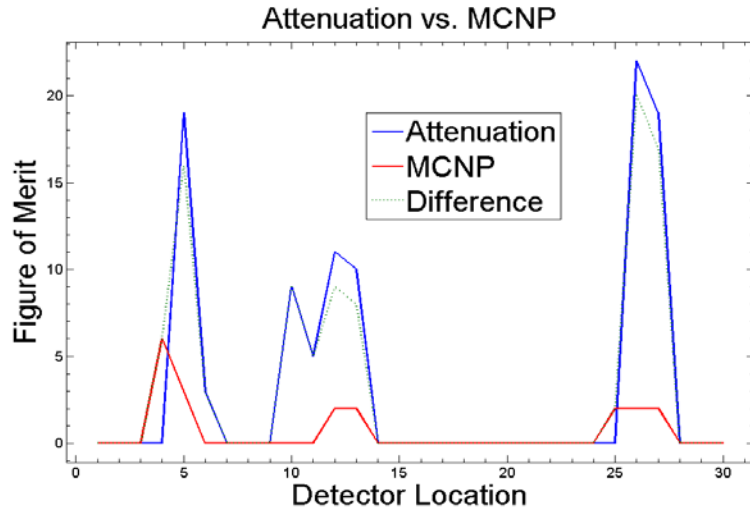


**Figure 19:** Frequency of occurrence of optimal locations for three detectors for the top 30 pairs of detector locations from the algorithm for both the 2-D attenuation and MCNP models. The difference between the algorithm results when using each model is also shown.

#### 4.4 Four Detector Model

The final problem investigated in this research was the four detector problem. Again, an additional outside loop was added to the optimal detector algorithm. This increased the model run time to just over an hour. This is significant because one of the goals of this work is to decrease the amount of computational time that MCNP requires. The result of the fourth

detector was interesting in that the two results are almost identical again. The concrete walled office still has one detector but the rest of the detectors have now pushed to the middle of the room and away from the corners.

The 2-D attenuation model produced optimal locations of 4-13-17-28 as shown on the left side of Figure 20. The outside corners are no longer indicated as optimal placement locations. Additionally, the tolerance had to be lowered to .01 percent in order to identify significant differences in detector placements, similar to the results using the MCNP model.

The MCNP model produced an optimal detector placement of 3-12-16-27, as shown on the right side of Figure 20. The tolerance was reduced again by approximately two orders of magnitude due to the overlap of detectors. It appears as though the detectors are now following the electrical boxes which run down the center of the room (see Figure 7).

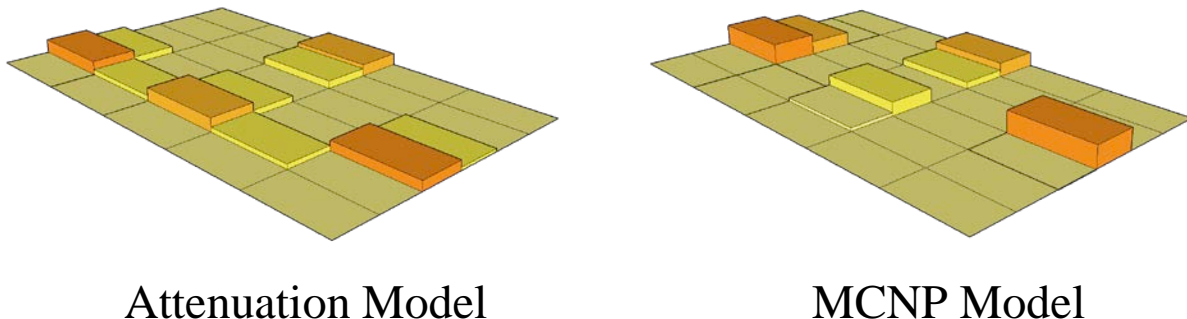


**Figure 20: A side by side representation of the 2-Dattenuation model versus the MCNP model with 4 detectors.**

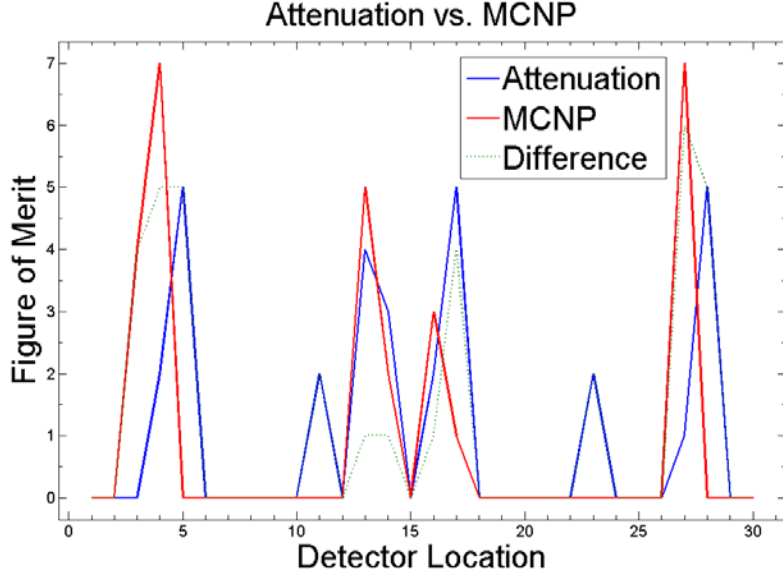


**Figure 21: Frequency of occurrence of optimal locations for four detectors for the top 30 pairs of detector locations from the algorithm for both the 2-D attenuation and MCNP models. The difference between the algorithm results when using each model is also shown.**

Of note, a five detector model was run utilizing both algorithms. Each run took over 6 hours and produced results of little significance due to overlap of detector FOV. The results were consistently between 5 and 6 on the intensity scale, resulting in a near uniform distribution of preferred locations.

#### 4.5 Error

Comparison of the MCNP model to experimental measurements was required in order to determine whether the MCNP model could be used as a surrogate for experimental measurements at all 900 source-detector location combinations, which would have been an extremely time consuming process. The comparison was performed by taking the total count in the full energy peak from two grid locations and then dividing one grid location by the other, yielding a ratio between the two positions for a given model. Positions 18 and 24, with the source in position 30, were utilized for this analysis because the MCNP model produced low

relative error at these particular locations with short run times. Other locations could be used later, but would require longer run time to produce a low relative error. Figure 22 shows the energy spectra from the MCNP model. The two peaks at 662 keV were used to determine the ratio. The same peak ratio from the experimental results was compared with the peak ratio from the MCNP model. The results for the ratio of position 18 to position 24 for both the experiment and MCNP are shown in Table 1.

To determine the uncertainty in these ratios, MCNP relative error was used. Relative error is the standard deviation over the mean for a particular energy bin within the MCNP model. The relative error was determined for both the experiment and the MCNP model as shown in Table 2. Twice the relative error was used to determine the confidence intervals shown in Table 1

**Table 1: A comparison of simulated and experimental detector responses and their uncertainties.**

MCNP Peak Ratio	Experimental Peak Ratio
$0.0698 \pm 0.0134$	$0.0744 \pm 0.0073$

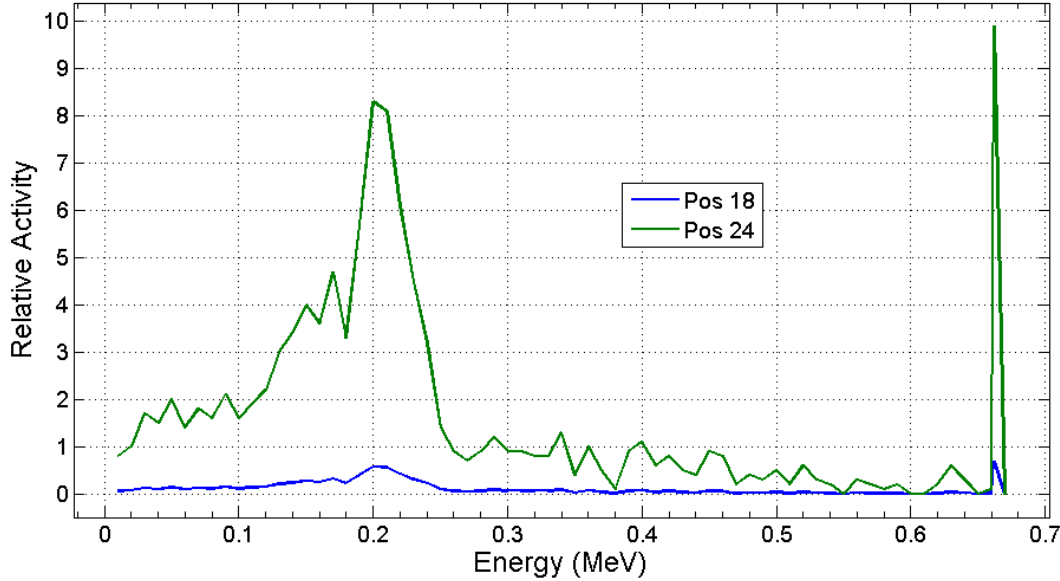


Figure 22: Comparison of the MCNP simulated detector responses from grid locations 18 and 24.

Table 2: Simulated and experimental relative uncertainties for detectors placed in grid locations 18 and 24 (Figure 15).

Data Set	Relative Error
MCNP $10^9$ Tracks (Calculated from MCNP) Position 18	0.0436
Experimental (Calculated for GammaVision) Position 18	0.0049
MCNP $10^9$ Tracks (Calculated from MCNP) Position 24	0.096
Experimental (Calculated for GammaVision) Position 24	0.00389

The results demonstrated that the current MCNP model could be utilized to replicate the experimental results because of the low relative error and the ratios matched within two standard deviations.

## 4.6 Analysis of the Compton Back Scatter Region

As a result of the multi-detector placement models producing an output which calculated the optimal placement for detectors close to the steel electrical boxes down the center of the basement, a decision was made to examine scattering off the objects in the room. A MCNP model was developed in order to try and determine some of the effects of the attenuating objects in the basement on the photons in order to determine their scattering effects on the nearby detectors. Additionally, the information could provide details into whether or not SNM could be detected using gamma energies outside the photopeak regions. The results of the MCNP tallies might then also be used later to validate an expansion of a two dimensional MATLAB program which could predict source-specific spectra on each detector in the room.

The MCNP tallies produced interesting, but not unexpected results within the first two to three detector grids. However as the distance increased from the source, the effects of attenuation and the declining interaction probability resulted in extremely long computational time in order to produce a spectrum. These long computational times validate the need for the project. Due to the extended run times a decision was made to utilize 24 hrs runs utilizing a million particles. While the results still fell off outside three grid squares, analysis could still be made within that circumference.

As per Figure 15, the source was placed in the lower right hand corner and spectra was taken on the 29 detectors consolidating energies into 70 bins. The MCNP card can be seen in Appendix 4. Each NaI detector was placed in the center of each grid square within the MCNP model. By binning the energies of each particle, the MCNP model was able to produce a spectrum at each grid location similar to the one shown in Figure 23 except with 70 bins.

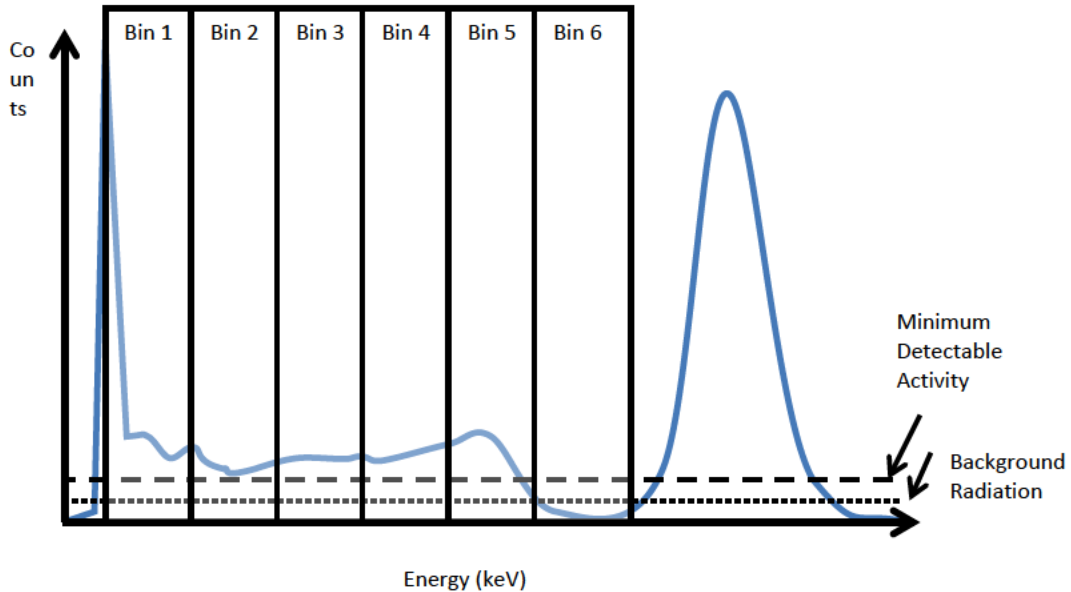


**Figure 23: Graphical representation of how particle energies were binned within MCNP.**

The results produced from the MCNP Model are shown below in Figure 24, Figure 25, and Figure 26. Figure 24 is one grid square left of the red source seen in Figure 9. Figures 25 and 26 continue the model to the left of that grid location. Once, outside the circumference of the last detector error simply becomes too high for spectra to be reliable. This can be resolved with much longer run time or more particles in MCNP.

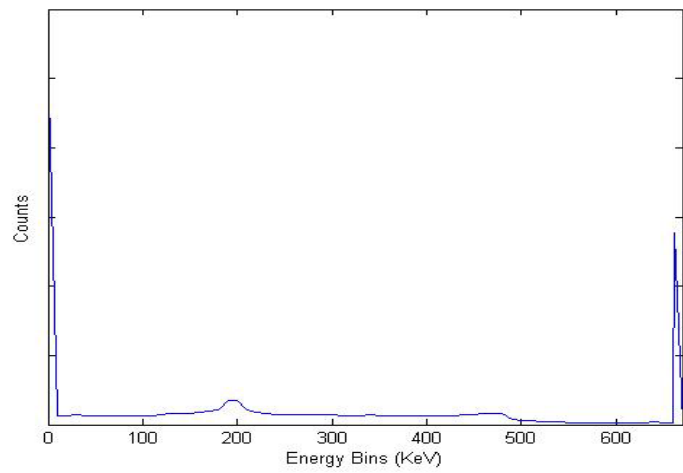


**Figure 24:** Detector 24 spectra from a billion particle MCNP F8 Tally

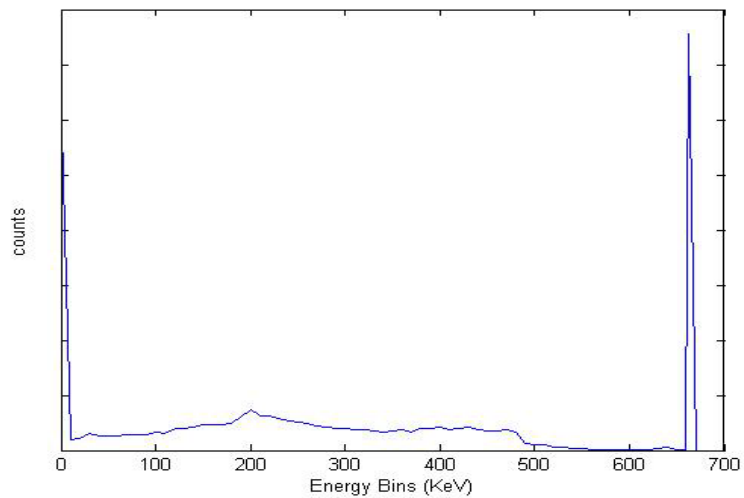


**Figure 25:** Detector 18 spectra from a billion particle MCNP F8 Tally

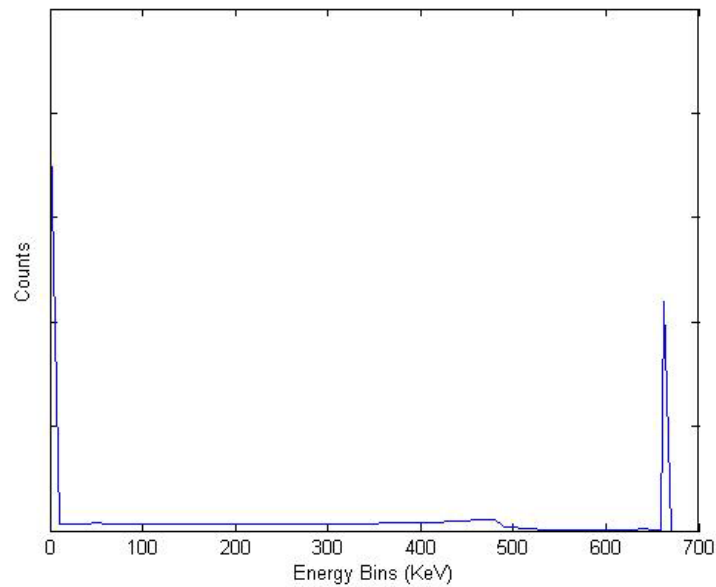


**Figure 26:** Detector 17 spectra from a billion particle MCNP F8 Tally

## VI. Conclusions and Recommendations for Future Study

The purpose of this research was two-fold. The first objective was to develop an algorithm to determine an optimal detector emplacement strategy based on the number of detectors available. The second objective was to determine whether the 2-D photon attenuation analytical transport model could favorably replicate the results of an MCNP model for application in this detector placement optimization algorithm. The MCNP model was validated with experimental measurements. The optimization algorithm was then tested using both the 2-D attenuation and MCNP models. The 2-D model is able to replicate the MCNP results in a fraction of the time. Additionally, the 2-D photon attenuation analytical transport model can predict optimal detector locations with the same proficiency as the MCNP model.

The most significant discovery is the 2-D attenuation model can predict optimal detector location much faster than MCNP. Since faster predictions are important in achieving faster detection methodologies, the 2-D attenuation model promises to speed up the process of source detection significantly. Though this research hoped to utilize the backscatter region as a method of detection, the low energy gamma attenuation through a large area required extensive simulation times. To achieve better results, the methodologies need to become part of a larger strategy incorporating faster models to predict detector responses from radiation sources. This research serves as an additional step in decreasing those run times.

The overarching project through which this research was conducted aims to identify special nuclear material utilizing a combination of Polarimetric-Hyperspectral imaging (PHSI) and traditional radionuclide identification. The results of this research will allow for optimal placement of the detectors to acquire a source. The PHSI will provide the material surrounding

the source to enhance the modeling of attenuated spectra. The advantage of the 2-D model is to speed up the acquisition time.

Future work in this area includes adapting the algorithm and models to utilize more than one type of gamma detection system. Additionally, the algorithm might be adapted for use with detectors that have neutron detection capabilities. However, the most significant expansion of this work would be to include the Compton continuum region. Previous work in this area has shown that particular sources can be detected using only the Compton region. If a database was built to predict detector behaviors in this region for various energies and materials, the algorithm could become even more useful in determining optimal placement of detection systems focusing primarily on attenuated photons. A preliminary discussion of the theoretical implementation of Compton scattering in the attenuation model is included in Appendix D.

## VII. Appendices

### Appendix A

Input file for a F5 tally in simulation geometry.

```
c cell cards
10 204 -0.001225 -1 2 3 4 5 10 12 13 15 16 17 18 19 imp:p=1
20 6000 -2.35 -2 imp:p=1 $ Columns down the middle
30 6000 -2.35 -3 imp:p=1
40 6000 -2.35 -4 imp:p=1
50 6000 -2.35 -5 imp:p=1 $ Column at the front of Mezzanine
c 70 2000 -2.35 -7 imp:p=1 $ floor
100 4000 -1.7 -10 imp:p=1 $ graphite box
120 204 -0.001225 -12 imp:p=1 $ air bubble inside office
130 6000 -2.35 -13 12 imp:p=1 $ office wall
c 140 5000 -7.874 -14 imp:p=1 $ electrical box
150 5000 -7.874 -15 imp:p=1 $ electrical box middle
160 5000 -7.874 -16 imp:p=1 $ electrical box right
170 5000 -7.874 -17 imp:p=1 $ Electrical box left
180 2000 -7.874 -18 imp:p=1 $ Electrical Box Empty
190 5000 -7.874 -19 imp:p=1 $ Electrical Bax Full
c 200 9999 -2.350 -20 imp:p=1 $ Test Point detector
210 0 1 imp:p=0 $ Outside Universe

c surface cards
1 rpp 0 2136 0 1266 0 350 $ Mezzanine
2 rpp 60 99 716 755 0 350 $ Column
3 rpp 739 778 716 755 0 350 $ Column
4 rpp 1379 1418 716 755 0 350 $ Column
5 rpp 1550 1589 0 39 0 350 $ Column
c 7 rpp 0 2125 0 1350 -30 0 $ Concrete Floor
10 rpp 1620 1750 180 310 0 200 $ Graphite Box
12 rpp 755 1250 40 511 0 240 $ Air inside Office
13 rpp 725 1280 0.01 541 0.01 240 $ Office Wall
15 rpp 1608 2063 795 845 0 240 $ Right Electric Box
16 rpp 1028 1368 795 845 0 240 $ Middle Electric Box
17 rpp 448 788 795 845 0 240 $ Left Electrical Box
18 rpp 313 443 1125 1174.99999 0 240 $ Electrical Box in Back Corner Empty
19 rpp 313 443 1175 1225 0 240 $ Electrical Box Full in Back Corner
c 20 rpp 0 192 0 116 0 350 $Test Point Detector

c data cards
mode p
nps 100000
totnu
m2000 1001 2 8016 1
m4000 6000 -1
m5000 26000 -0.65395 $Steel
24000 -0.17000
28000 -0.12
25055 -0.02
14000 -0.01
```

```

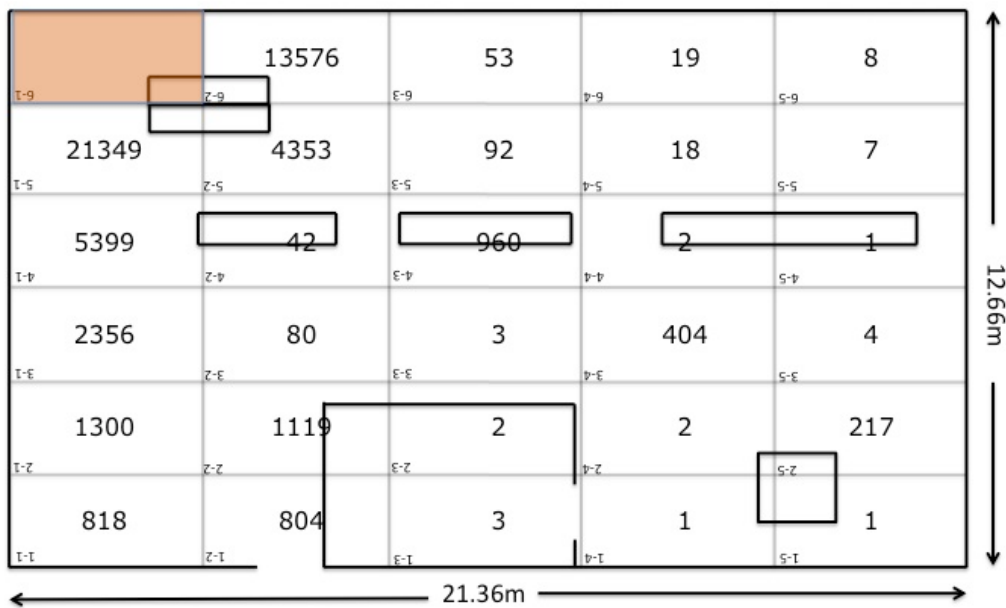
15031 -0.00045
16032 -0.0003
6012 -0.0003
42000 -0.025
m204 8016 1 7014 4
m6000 1001. -0.0221 $Concrete
 6000. -0.002484
 8000. -0.574930
11000. -0.015208
12000. -0.001266
13000. -0.019953
14000. -0.304627
19000. -0.010045
20000. -0.042951
26000. -0.006435
c m9999 1001 2 8016 2 $Test Material
c Cobalt Point Source
sdef pos 213.6 1160.5 150 erg=.662
c
f5:p 213.6 105.5 150 30
c 640.8 105.5 150 30
c 1068 105.5 150 30
c 1495.2 105.5 150 30
c 1922.4 105.5 150 30
c 213.6 316.5 150 30
c 640.8 316.5 150 30
c 1068 316.5 150 30
c 1495.2 316.5 150 30
c 1922.4 316.5 150 30
c 213.6 527.5 150 30
c 640.8 527.5 150 30
c 1068 527.5 150 30
c 1495.2 527.5 150 30
c 1922.4 527.5 150 30
c 213.6 738.5 150 30
c 640.8 738.5 150 30
c 1068 738.5 150 30
c 1495.2 738.5 150 30
c 1922.4 738.5 150 30
c 213.6 949.5 150 30
c 640.8 949.5 150 30
c 1068 949.5 150 30
c 1495.2 949.5 150 30
c 1922.4 949.5 150 30
c 640.8 1160.5 150 30
c 1068 1160.5 150 30
c 1495.2 1160.5 150 30
c 1922.4 1160.5 150 30
c
print

```

## Appendix B

### Counts from Individual 1 Detector MCNP F4 Tallies

## Position 1



## Position 2

5117			5179	1294	563
4078	21712		4356	1264	580
2580	55	2752	72	9	
1532	32	857	28	12	
35	17	24	44	10	
18	8	12	13	2	

21.36m

12.66m

## Position 3

950	5142		5088	1271
1198	4383	21390	4309	1268
995	133	206	2530	12
29	161	5	38	783
17	29	13	13	591
13	8	15	7	11

21.36m

12.66m

## Position 4

20	1311	5086		5098
539	1289	4384	20970	4503
20	29	65	5552	38
14	32	0	2356	59
343	9	4	1327	45
9	1	3	874	28
8	559	1265	5073	
287	572	1260	4194	21414
7	461	56	2622	16
4	8	281	47	18
2	1	2	22	15
1	0	1	10	7

21.36m ← →

12.66m ↑ ↓

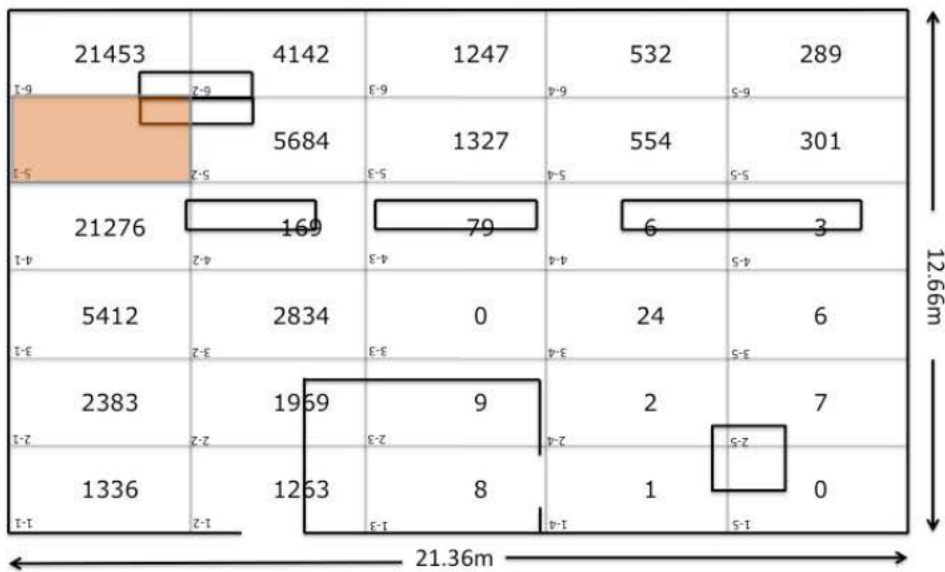
## Position 5

8	559	1265	5073	
287	572	1260	4194	21414
7	461	56	2622	16
4	8	281	47	18
2	1	2	22	15
1	0	1	10	7

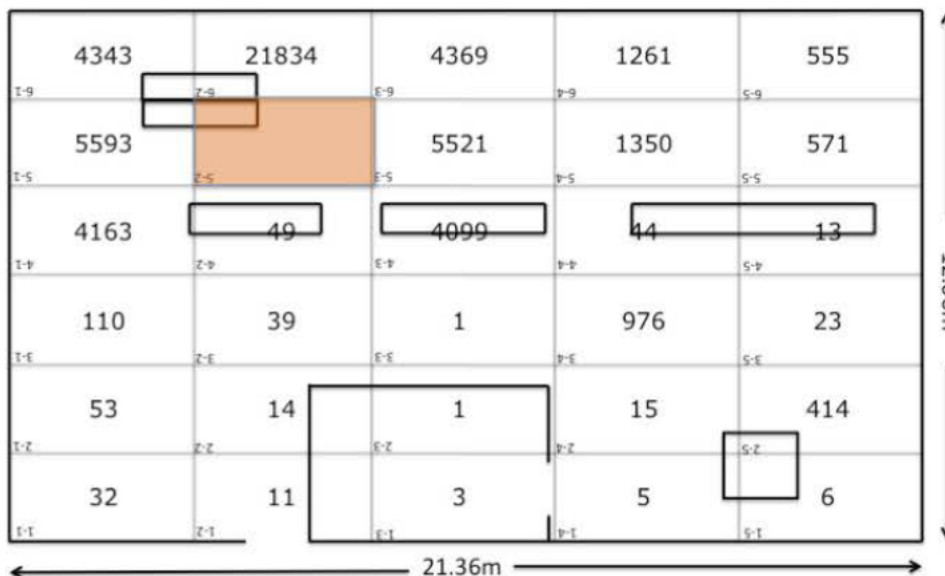
21.36m ← →

12.66m ↑ ↓

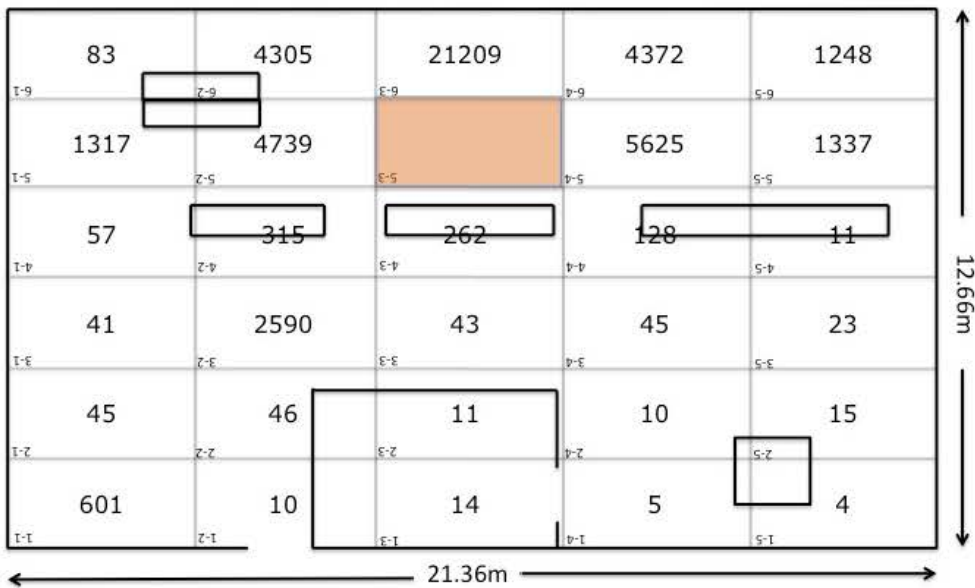
## Position 6



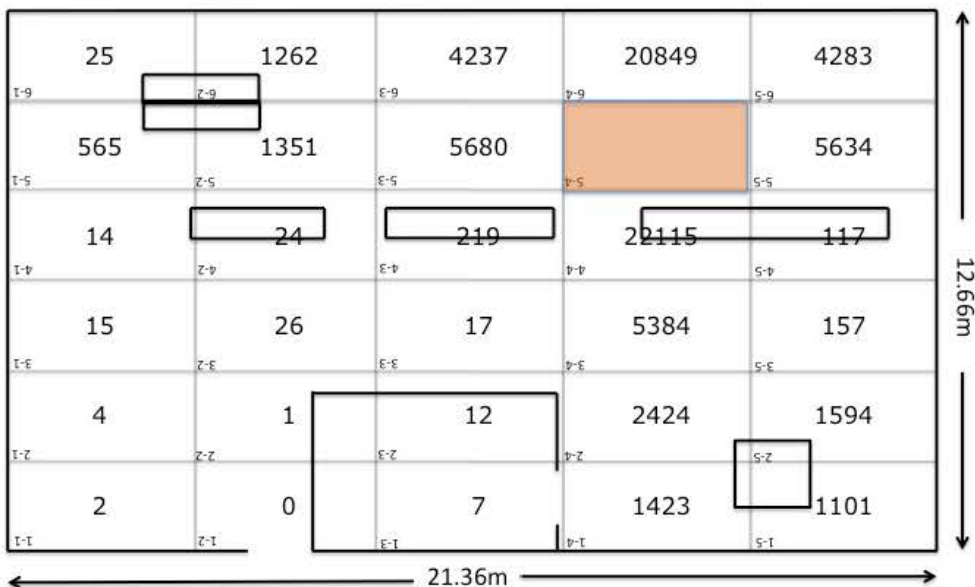
## Position 7



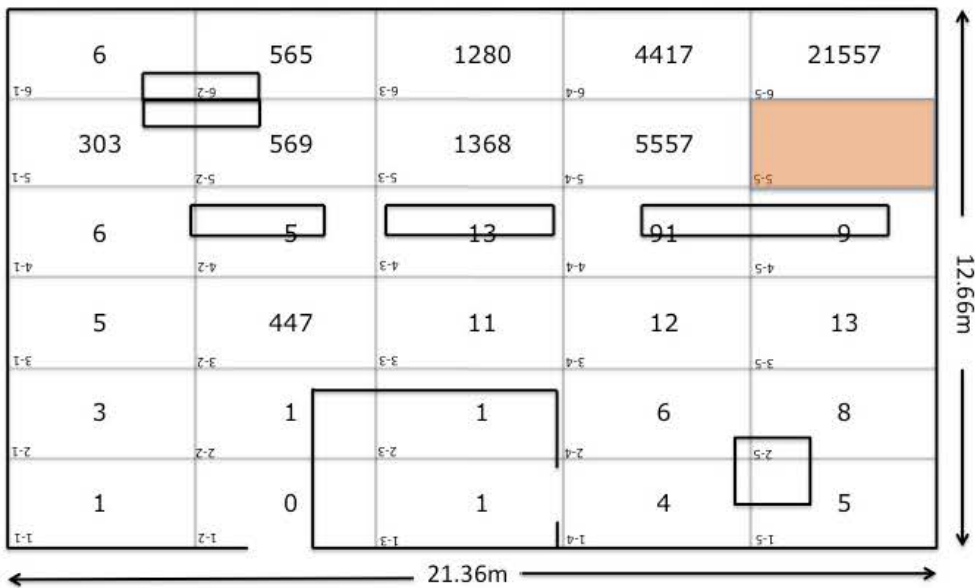
## Position 8



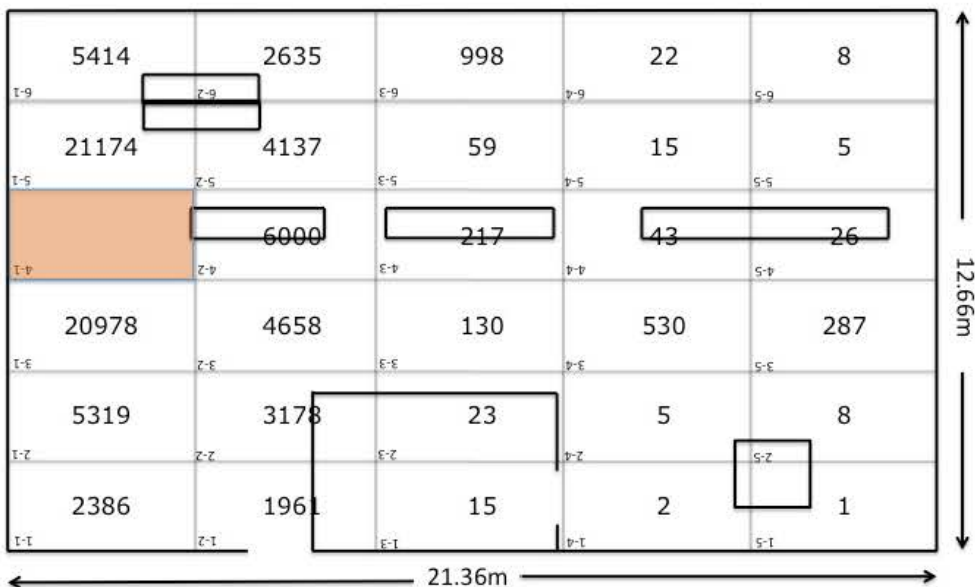
## Position 9



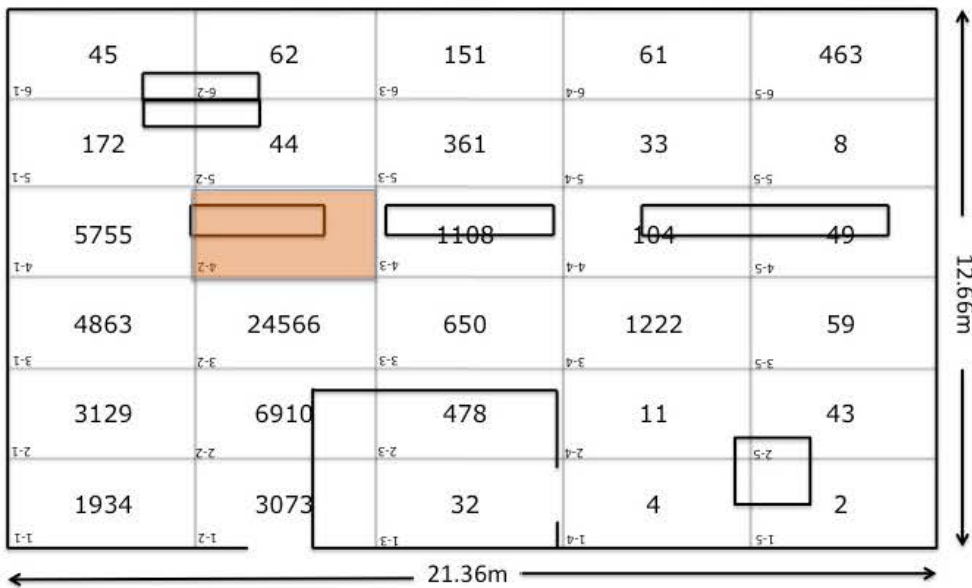
## Position 10



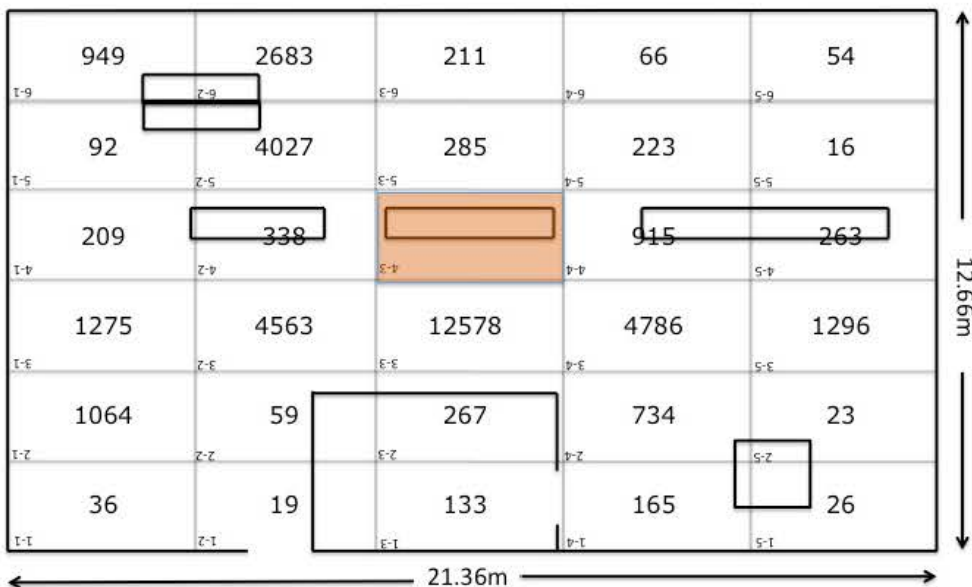
## Position 11



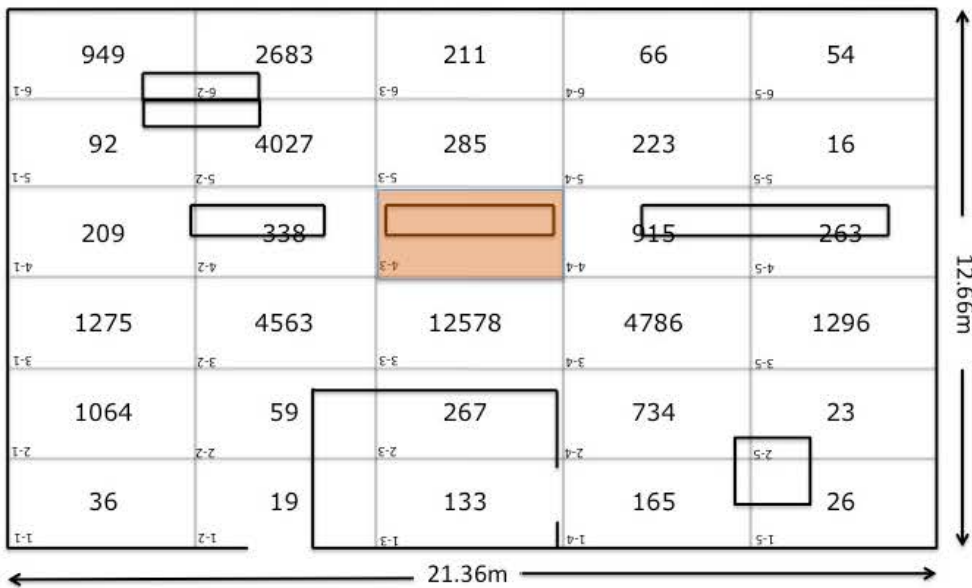
## Position 12



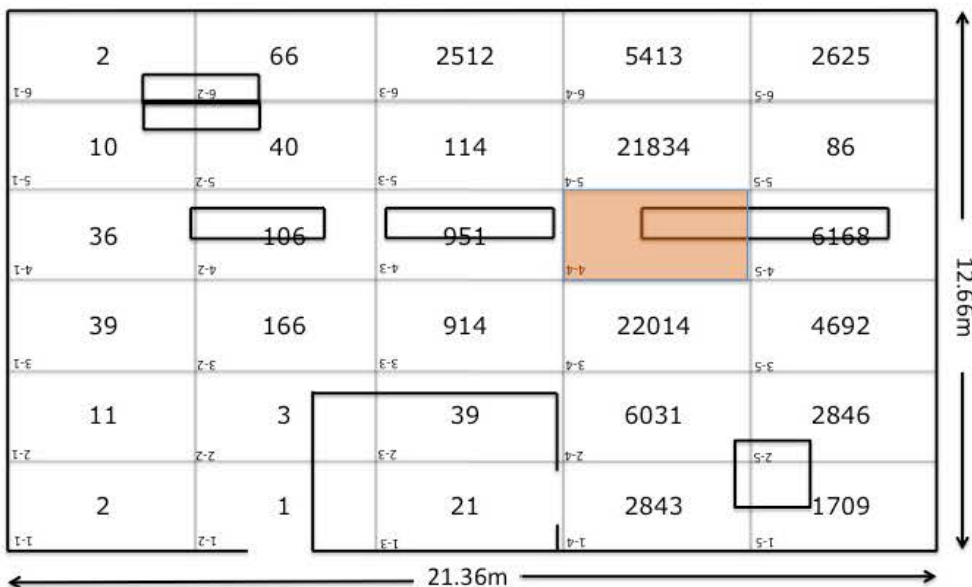
## Position 13



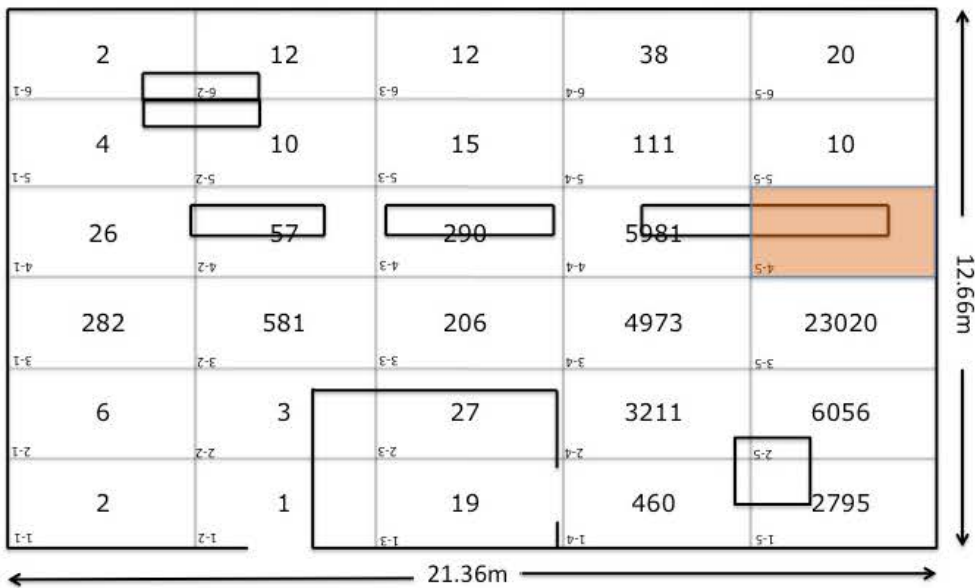
## Position 13



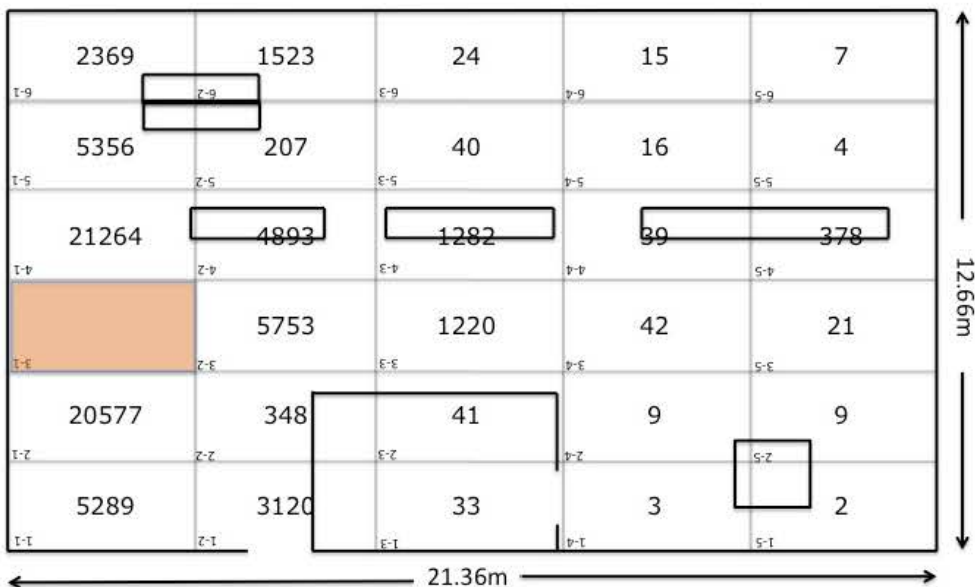
## Position 14



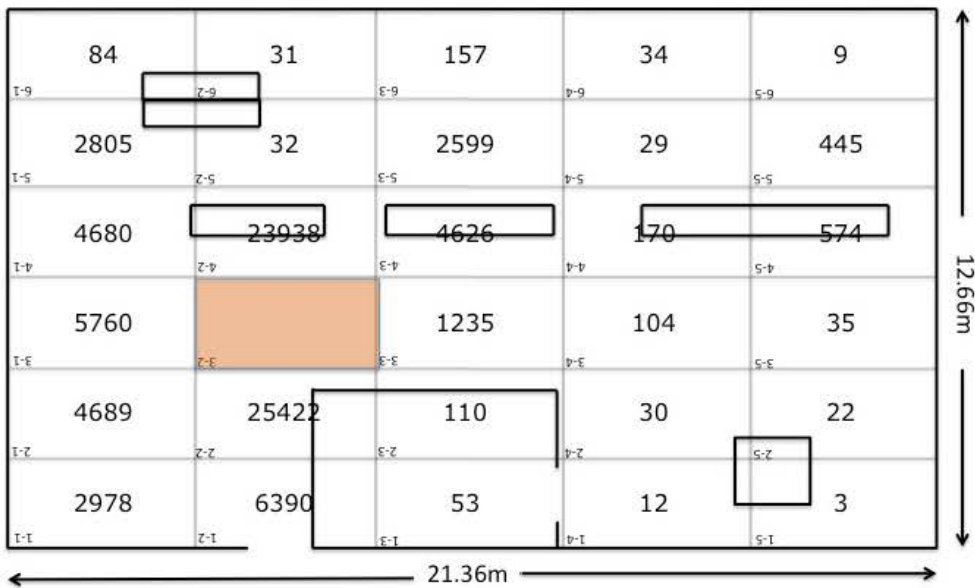
## Position 15



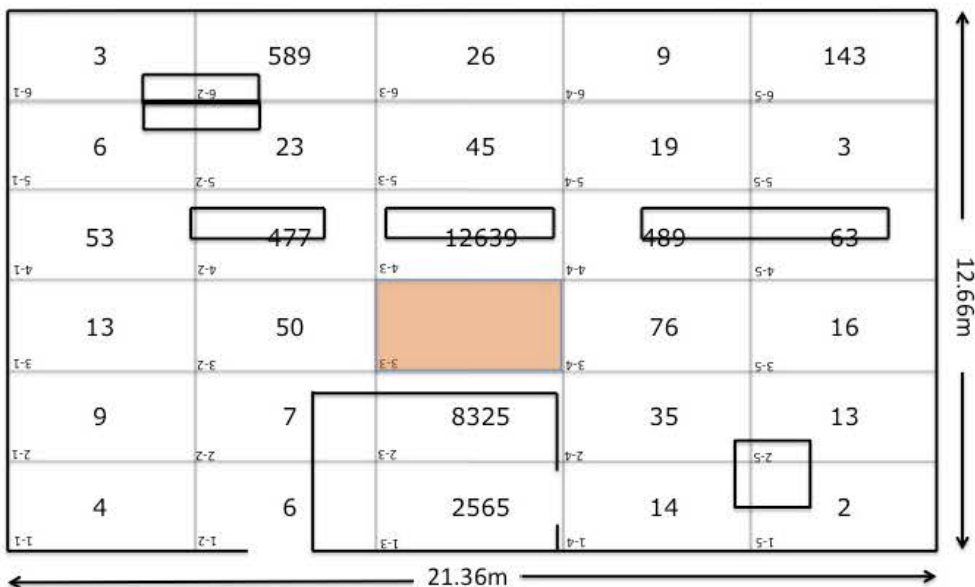
## Position 16



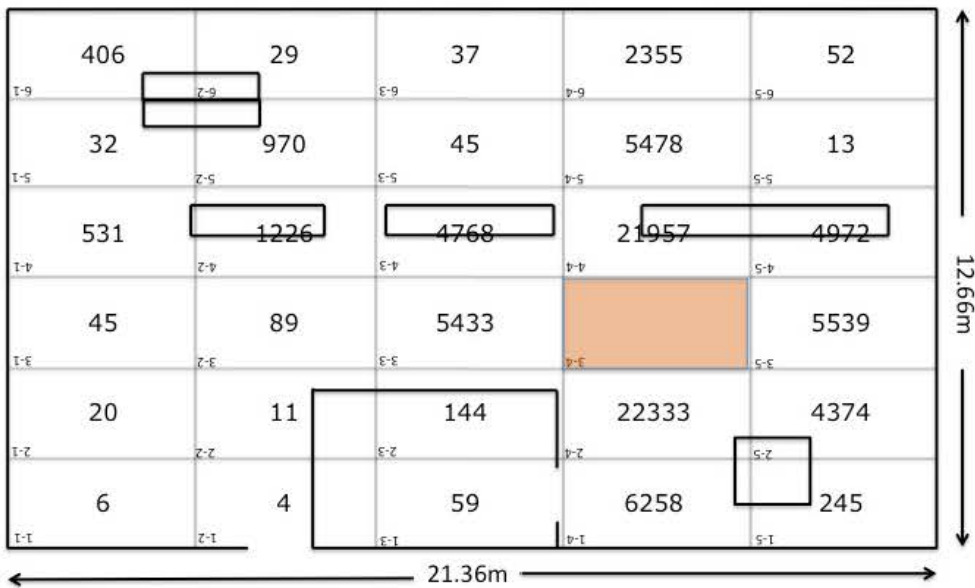
## Position 17



## Position 18



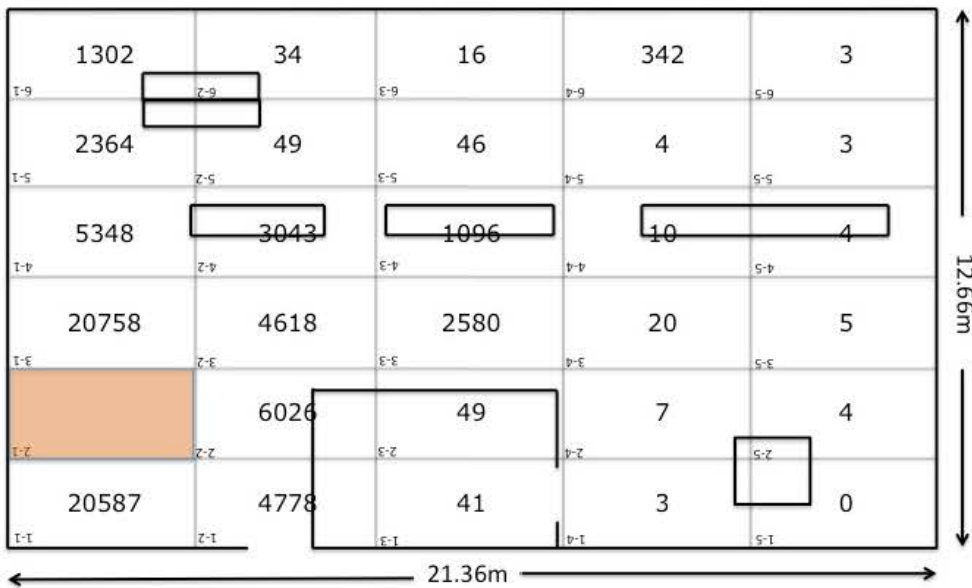
## Position 19



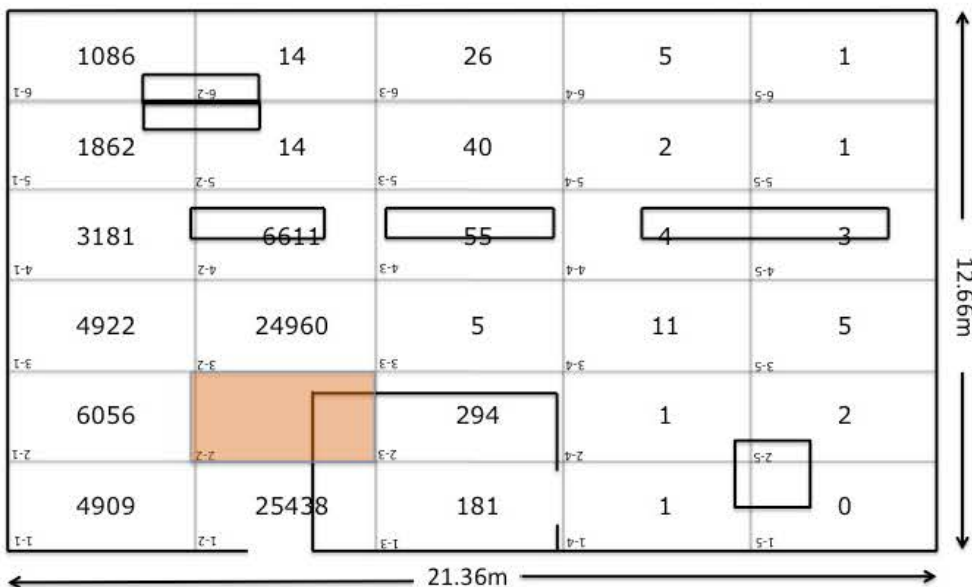
## Position 20



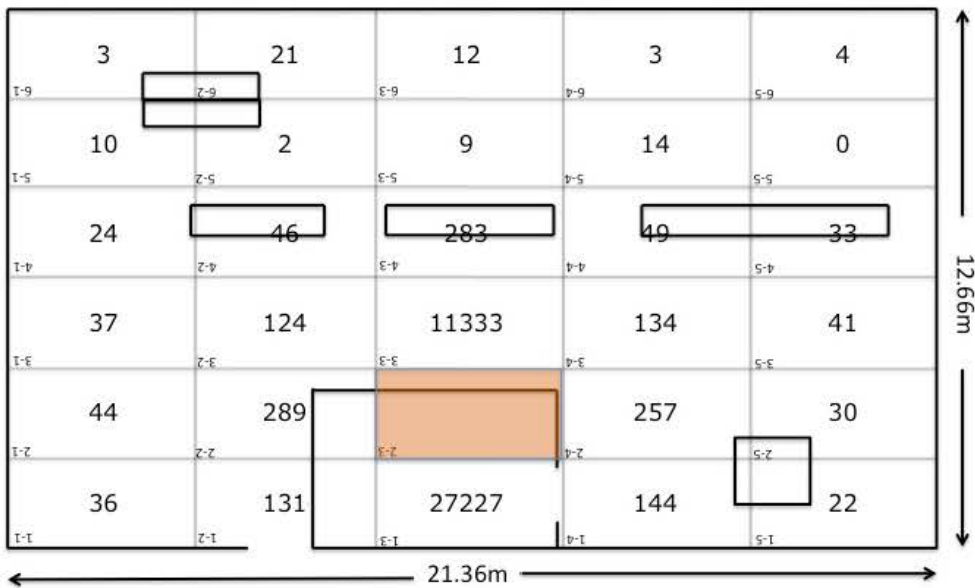
## Position 21



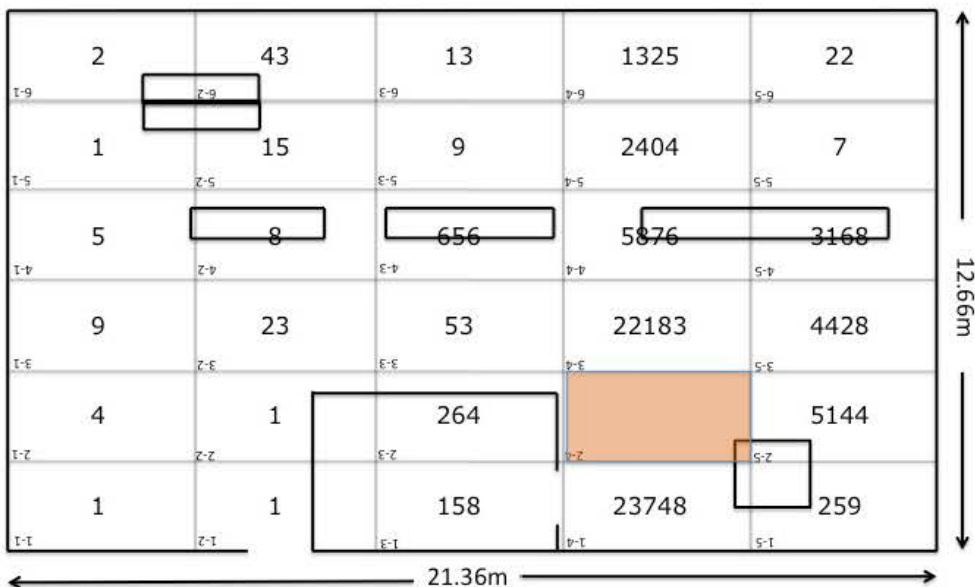
## Position 22



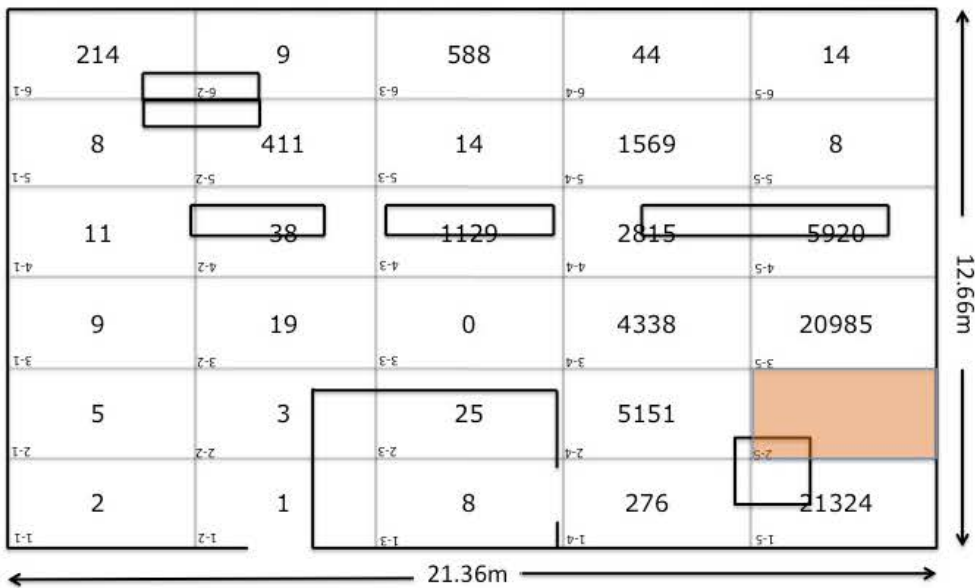
## Position 23



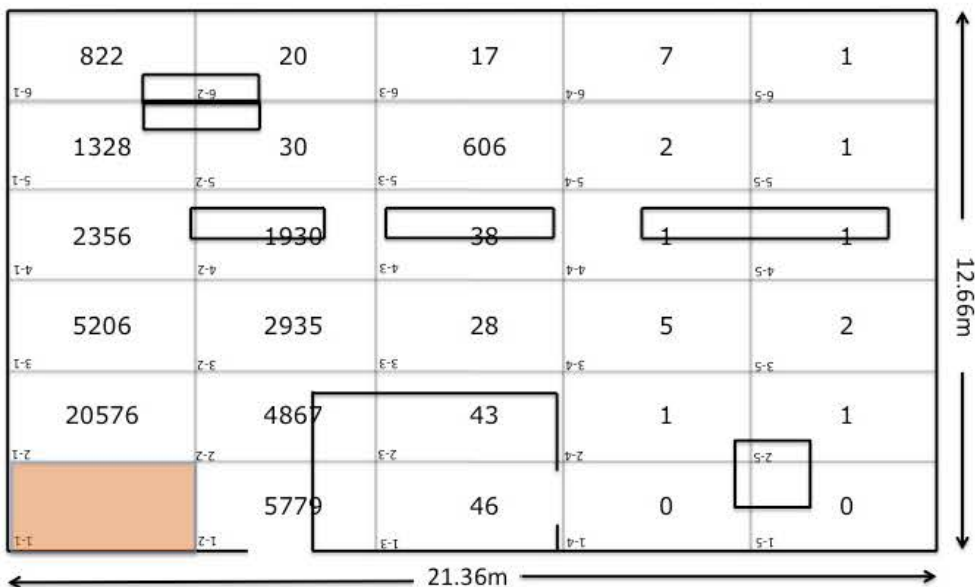
## Position 24



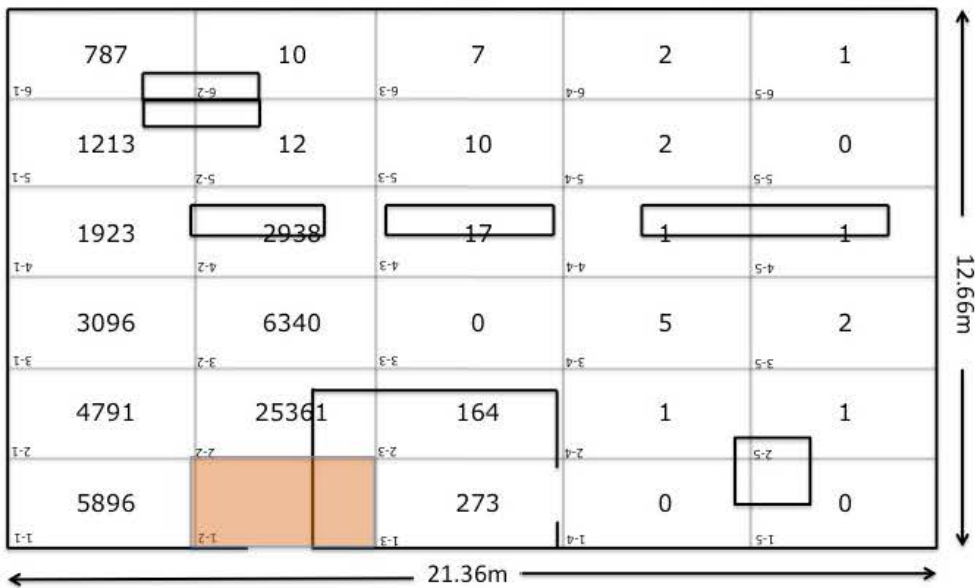
## Position 25



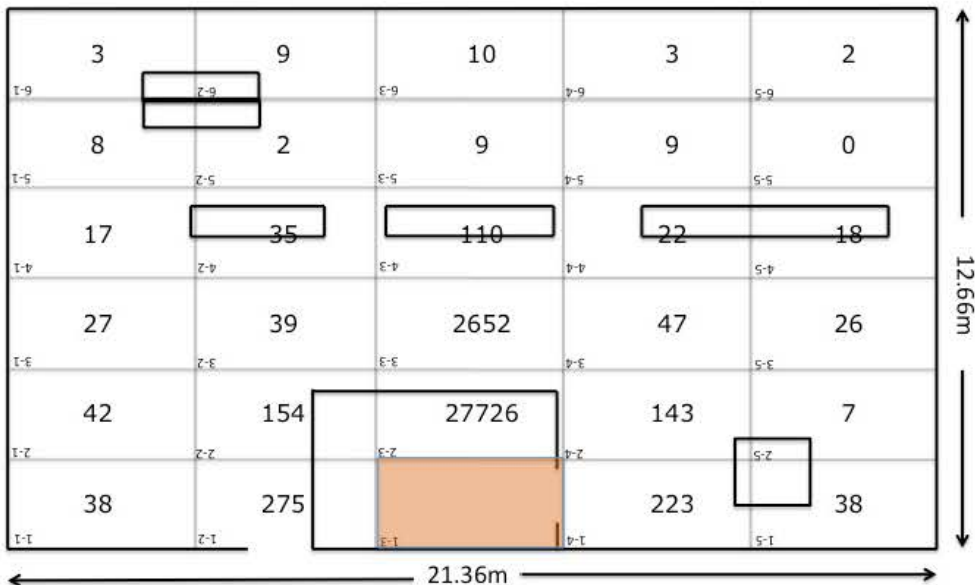
## Position 26



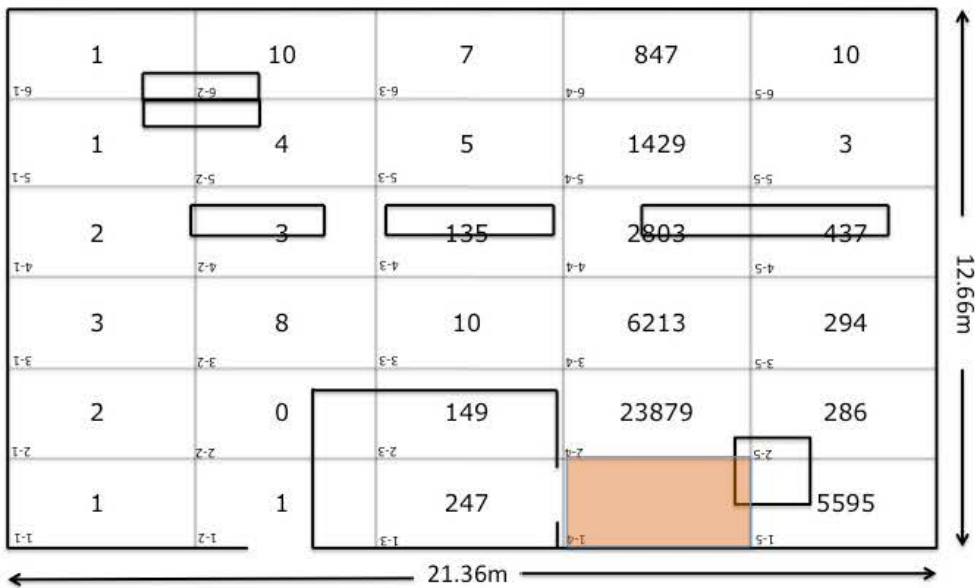
## Position 27



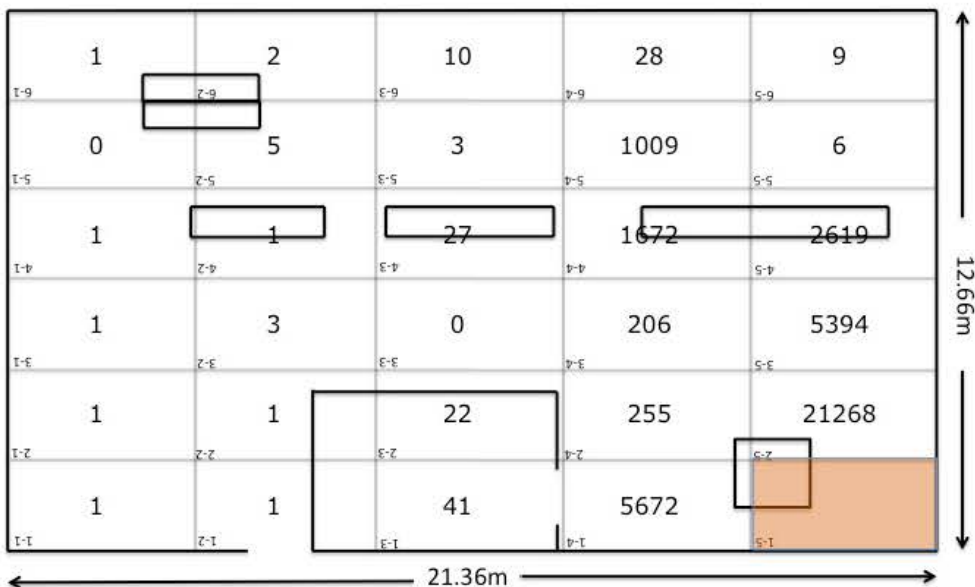
## Position 28



## Position 29



## Position 30



## Appendix C

A sample input file for a F8 tally for spectra calculations.

```
1- Backscatter Bins
2- c cell cards
3- 10 204 -0.001225 -1 2 3 4 5 10 12 13 15 16 17 18 19 &
4-     21 22 23 24 25 26 27 28 29 30 31 32 33 34 35 36 &
5-     37 38 39 40 41 42 43 44 45 48 49 imp:p=1
6- 20 6000 -2.35 -2 imp:p=1 $ Columns down the middle
7- 30 6000 -2.35 -3 imp:p=1
8- 40 6000 -2.35 -4 imp:p=1
9- 50 6000 -2.35 -5 imp:p=1 $ Column at the front of Mezzanine
10- c 70 2000 -2.35 -7 imp:p=1 $ floor
11- 100 4000 -1.7 -10 imp:p=1 $ graphite box
12- 120 204 -0.001225 -12 imp:p=1 $ air bubble inside office
13- 130 6000 -2.35 -13 12 imp:p=1 $ office wall
14- c 140 5000 -7.874 -14 imp:p=1 $ electrical box
15- 150 5000 -7.874 -15 imp:p=1 $ electrical box middle
16- 160 5000 -7.874 -16 imp:p=1 $ electrical box right
17- 170 5000 -7.874 -17 imp:p=1 $ Electrical box left
18- 180 2000 -7.874 -18 imp:p=1 $ Electrical Box Empty
19- 190 5000 -7.874 -19 imp:p=1 $ Electrical Bax Full
20- c 200 9999 -2.350 -20 imp:p=1 $ NaI detector
21- 201 9999 -2.350 -21 imp:p=1 $ NaI detector
22- 202 9999 -2.350 -22 imp:p=1 $ NaI detector
23- 203 9999 -2.350 -23 imp:p=1 $ NaI detector
24- 204 9999 -2.350 -24 imp:p=1 $ NaI detector
25- 205 9999 -2.350 -25 imp:p=1 $ NaI detector
26- 206 9999 -2.350 -26 imp:p=1 $ NaI detector
27- 207 9999 -2.350 -27 imp:p=1 $ NaI detector
28- 208 9999 -2.350 -28 imp:p=1 $ NaI detector
29- 209 9999 -2.350 -29 imp:p=1 $ NaI detector
30- 210 9999 -2.350 -30 imp:p=1 $ NaI detector
31- 211 9999 -2.350 -31 imp:p=1 $ NaI detector
32- 212 9999 -2.350 -32 imp:p=1 $ NaI detector
33- 213 9999 -2.350 -33 imp:p=1 $ NaI detector
34- 214 9999 -2.350 -34 imp:p=1 $ NaI detector
35- 215 9999 -2.350 -35 imp:p=1 $ NaI detector
36- 216 9999 -2.350 -36 imp:p=1 $ NaI detector
37- 217 9999 -2.350 -37 imp:p=1 $ NaI detector
38- 218 9999 -2.350 -38 imp:p=1 $ NaI detector
39- 219 9999 -2.350 -39 imp:p=1 $ NaI detector
40- 220 9999 -2.350 -40 imp:p=1 $ NaI detector
41- 221 9999 -2.350 -41 imp:p=1 $ NaI detector
42- 222 9999 -2.350 -42 imp:p=1 $ NaI detector
43- 223 9999 -2.350 -43 imp:p=1 $ NaI detector
44- 224 9999 -2.350 -44 imp:p=1 $ NaI detector
45- 225 9999 -2.350 -45 imp:p=1 $ NaI detector
46- 226 9999 -2.350 -46 imp:p=1 $ NaI detector
47- 227 9999 -2.350 -47 imp:p=1 $ NaI detector
48- 228 9999 -2.350 -48 imp:p=1 $ NaI detector
49- 229 9999 -2.350 -49 imp:p=1 $ NaI detector
```

```

50- 250 0 1      imp:p=0  $ Outside Universe
51-
52- c surface cards
53- 1 rpp 0 2136 0 1266 0 350      $ Mezzanine
54- 2 rpp 60 99 716 755 0 350      $ Column
55- 3 rpp 739 778 716 755 0 350      $ Column
56- 4 rpp 1379 1418 716 755 0 350      $ Column
57- 5 rpp 1550 1589 0 39 0 350      $ Column
58- c 7 rpp 0 2125 0 1350 -30 0      $ Concrete Floor
59- 10 rpp 1620 1750 180 310 0 200      $ Graphite Box
60- 12 rpp 755 1250 40 511 0 240      $ Air inside Office
61- 13 rpp 725 1280 0.01 541 0.01 240      $ Office Wall
62- 15 rpp 1608 2063 795 845 0 240      $ Right Electric Box
63- 16 rpp 1028 1368 795 845 0 240      $ Middle Electric Box
64- 17 rpp 448 788 795 845 0 240      $ Left Electrical Box
65- 18 rpp 313 443 1125 1174.99999 0 240      $ Electrical Box in Back Corner Empty
66- 19 rpp 313 443 1175 1225 0 240      $ Electrical Box Full in Back Corner
67- c 20 rcc 213.6 105.5 150 30 0 7.62 3.81 $NaI Detector1
68- 21 rcc 640.8 105.5 150 30 0 7.62 3.81 $NaI Detector2
69- 22 rcc 1068 105.5 150 30 0 7.62 3.81 $NaI Detector3
70- 23 rcc 1495.2 105.5 150 30 0 7.62 3.81 $NaI Detector4
71- 24 rcc 1922.4 105.5 150 30 0 7.62 3.81 $NaI Detector5
72- 25 rcc 213.6 316.5 150 30 0 7.62 3.81 $NaI Detector6
73- 26 rcc 640.8 316.5 150 30 0 7.62 3.81 $NaI Detector7
74- 27 rcc 1068 316.5 150 30 0 7.62 3.81 $NaI Detector8
75- 28 rcc 1495.2 316.5 150 30 0 7.62 3.81 $NaI Detector9
76- 29 rcc 1922.4 316.5 150 30 0 7.62 3.81 $NaI Detector10
77- 30 rcc 213.6 527.5 150 30 0 7.62 3.81 $NaI Detector11
78- 31 rcc 640.8 527.5 150 30 0 7.62 3.81 $NaI Detector12
79- 32 rcc 1068 527.5 150 30 0 7.62 3.81 $NaI Detector13
80- 33 rcc 1495.2 527.5 150 30 0 7.62 3.81 $NaI Detector14
81- 34 rcc 1922.4 527.5 150 30 0 7.62 3.81 $NaI Detector15
82- 35 rcc 213.6 738.5 150 30 0 7.62 3.81 $NaI Detector16
83- 36 rcc 640.8 738.5 150 30 0 7.62 3.81 $NaI Detector17
84- 37 rcc 1068 738.5 150 30 0 7.62 3.81 $NaI Detector18
85- 38 rcc 1495.2 738.5 150 30 0 7.62 3.81 $NaI Detector19
86- 39 rcc 1922.4 738.5 150 30 0 7.62 3.81 $NaI Detector20
87- 40 rcc 213.6 949.5 150 30 0 7.62 3.81 $NaI Detector21
88- 41 rcc 640.8 949.5 150 30 0 7.62 3.81 $NaI Detector22
89- 42 rcc 1068 949.5 150 30 0 7.62 3.81 $NaI Detector23
90- 43 rcc 1495.2 949.5 150 30 0 7.62 3.81 $NaI Detector24
91- 44 rcc 1922.4 949.5 150 30 0 7.62 3.81 $NaI Detector25
92- 45 rcc 213.6 1160.5 150 30 0 7.62 3.81 $NaI Detector26
93- 46 rcc 640.8 1160.5 150 30 0 7.62 3.81 $NaI Detector27
94- 47 rcc 1068 1160.5 150 30 0 7.62 3.81 $NaI Detector28
95- 48 rcc 1495.2 1160.5 150 30 0 7.62 3.81 $NaI Detector29
96- 49 rcc 1922.4 1160.5 150 30 0 7.62 3.81 $NaI Detector30
97-
98- c data cards
99- mode p
100- nps 1000000000
101- totnu
102- m2000 1001 2 8016 1
103- m4000 6000 -1
104- m5000 26000 -0.65395 $Steel

```

```

105-      24000 -0.17000
106-      28000 -0.12
107-      25055 -0.02
108-      14000 -0.01
109-      15031 -0.00045
110-      16032 -0.0003
111-      6012 -0.0003
112-      42000 -0.025
113-      m204  8016  1   7014 4
114-      m6000 1001. -0.0221 $Concrete
115-      6000. -0.002484
116-      8000. -0.574930
117-      11000. -0.015208
118-      12000. -0.001266
119-      13000. -0.019953
120-      14000. -0.304627
121-      19000. -0.010045
122-      20000. -0.042951
123-      26000. -0.006435
124-      m9999 11023 -0.5  53127 -0.5 $NaI
125-      c Cobalt Point Source
126-      sdef pos 1922.4 949.5 150 erg=.662
127-      c
128-      f8:p 201 202 203 204 205 206 207 208 209 210 211 212 &
129-      213 214 215 216 217 218 219 220 221 222 223 224 &
130-      226 227 228 229           $ Energy depositio
131-      E8  0 1.e-5 .01 .02 .03 .04 .05 .06 .07 .08 .09 &
132-      .1 .11 .12 .13 .14 .15 .16 .17 .18 .19 .20 .21 .22 .23 .24 .25 &
133-      .26 .27 .28 .29 &
134-      .30 .31 .32 .33 .34 .35 .36 .37 .38 .39 &
135-      .40 .41 .42 .43 .44 .45 .46 .47 .48 .49 &
136-      .50 .51 .52 .53 .54 .55 .56 .57 .58 .59 &
137-      .60 .61 .62 .63 .64 .65 .66 .662

```

## Appendix D

### Theoretical Extension of 2 Dimensional Model to Validate Results

The possibility of getting around the long run times of the MCNP model could be solved thru the use of the 2 dimensional attenuation model. Again, with the objective being to see how each detector is influenced by the objects and walls of the room.

In order to simplify the problem several assumptions will need to be made. The first, assumption is that each detector is only influenced by the closest object to the detector itself. Additionally, one could only look at the closest face of the object in question to the detector in question.

Because the point attenuation kernel has the capability, progress has been made towards this project. First, Attenuation Kernel utilizes a 6x5 Matrix with the measurements of the center of each grid square in the room. Utilizing this matrix, and the dimensions of each object a nested loop was created to determine the closest objects and the closest face of that particular object. These calculations were then added to the already existing matrix to store the calculations to be called easier later. Now the matrix has assigned the closest face of the closest object.

Next was to calculate the percentage of photons hitting that face. Because we know the end points of the object we were able to calculate the percentage of the 360 degrees of the emitting source which could hit the face of the nearest object. This percentage again is stored as an additional 6x5 matrix. This is displayed graphically for one grid square below in Figure 13.

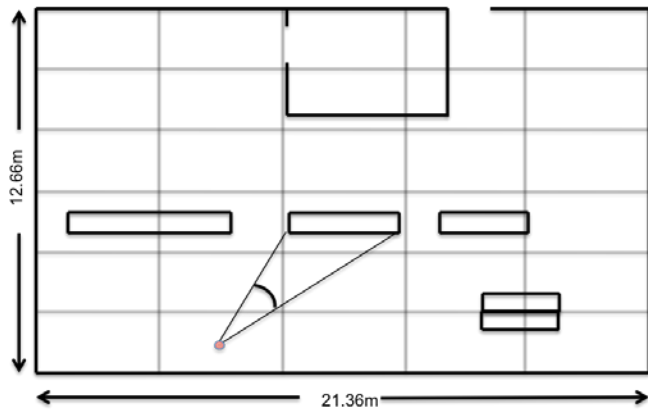


**Figure 27: Graphical representation of how the solid angle calculated percentage of incident photons on the face of the object for the 2D model.**

Now knowing the percentage of the isotropically emitting source which can hit the face of the nearest object, the 662 keV photons can be attenuated over the distance to the center of the face.

Next the angle of the photons hitting the face of the object was calculated to determine the angle of incident for each face. This was done to the center of each face and stored in additional 6x5 matrix.

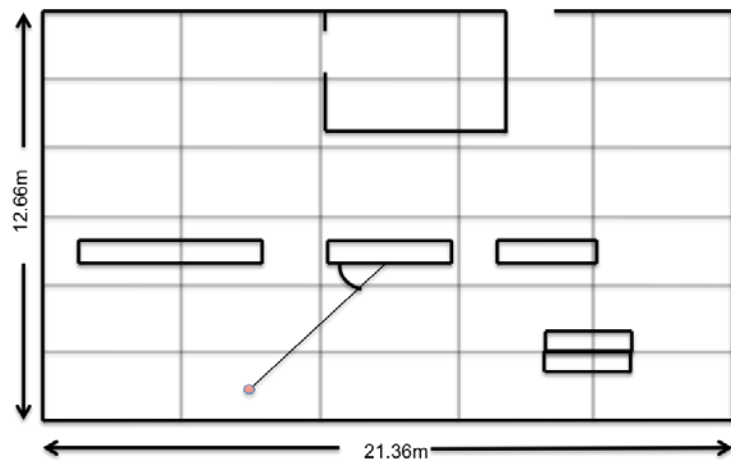


**Figure 28: Graphical representation of angle of incidence is assumed for the 2D model**

Currently the model has a list of 6x5 matrices which includes; center measurements of each grid square, closest object, face of the closest object, distance to the center of the nearest face, percentage of photons hitting the face and angle of incident to the face.

By making an assumption to simplify calculations is that every particle has the same angle of incidence hitting the face of the object. An addition to the current program could allow for the incorporation of the Klein-Nishina function. This will allow for the distribution of photon energies to be calculated, and with the energy, the point attenuation program could attenuate the photons thru the different materials and into the nearest detector producing a spectra. Yielding, some portion of scattered spectra into the 2-D program.

## Bibliography

- [1] Los Alamos National Lab, "MCNP — A General Monte Carlo N-Particle Transport Code, Version 5," in *Volume 1*, Berkley, Los Alamos National Lab, 2005.
- [2] Kansas State University, Dept. of Mechanical and Nuclear Engineering, "An MCNP Primer", [Online]. Available: <http://krex.ksu.edu/dspace/bitstream/handle/2097/15754/ShultisMCNP5.pdf?sequence=3>. [Accessed 02 06 2014].
- [3] R. S. Peterson, Experimental γ Ray Spectroscopy and Investigations of Environmental Radioactivity, Oak Ridge: Spectrum Techniques, 1996.
- [4] N. Reguigui, "Gamma ray Spectrometry, Practical Information", [Online]. Available: <http://www.cnstn.rnrt.tn/afra-ict/NAT/gamma/html/Gamma%20Spec%20V1.pdf> [Accessed 10 12 2014].
- [5] R. L. Heath, "Scintillation Spectrometry: Gamma-Ray Spectrum Catalogue", 2<sup>nd</sup> edition, IDO-16880-2, Phillips Petroleum Co. Atomic Energy Div., Idaho Falls, ID, 1964.
- [6] J. R. Lamarsh and A. J. Baratta, Introduction to Nuclear Engineering , third edition, Prentice Hall, 2001.
- [7] N. Sethi, "Modeling Sodium Iodide Detector Response Using Parametric Equations", Air Force Institute of Technology, MS Thesis, 2012.
- [8] T. Ospino, "Modeling Detector Response To Scattered Gamma Rays", Air Force Institute of Technology, MS Thesis, 2014.
- [9] G. F. Knoll, Radiation Detection and Measurement, Ann Arbor: Wiley, 2010.
- [10] P. L. Reeder and D. C. Stromswold, "Performance of Large NaI(Tl) Gamma-Ray Detectors Over Temperature -50 Degrees C to +60 Degrees C", PNNL-14735, Pacific Northwest National Laboratory, Richland, WA, 2004.
- [11] J. Zhang, J. Chen, B. Zou, Y. Zhang, "Modeling and Simulation of Polarimetric Hyperspectral Imaging Process", IEEE Transactions on Geoscience and Remote Sensing, Vol 50, No. 6, pp 2238 - 2253, 2012.
- [12] D. Reilly, N. Ensslin, H. Smith Jr., "Passive Nondestructive Assay of Nuclear Material", LA-UR-90-732, Los Alamos National Laboratory, Los Alamos, NM, 1991.
- [13] G. Gilmore, J.D. Hemingway, Practical gamma-ray spectrometry, Chichester: Wiley, 1995.

<b>REPORT DOCUMENTATION PAGE</b>			<i>Form Approved OMB No. 0704-0188</i>	
<p>The public reporting burden for this collection of information is estimated to average 1 hour per response, including the time for reviewing instructions, searching existing data sources, gathering and maintaining the data needed, and completing and reviewing the collection of information. Send comments regarding this burden estimate or any other aspect of this collection of information, including suggestions for reducing this burden to Department of Defense, Washington Headquarters Services, Directorate for Information Operations and Reports (0704-0188), 1215 Jefferson Davis Highway, Suite 1204, Arlington, VA 22202-4302. Respondents should be aware that notwithstanding any other provision of law, no person shall be subject to any penalty for failing to comply with a collection of information if it does not display a currently valid OMB control number. PLEASE DO NOT RETURN YOUR FORM TO THE ABOVE ADDRESS.</p>				
1. REPORT DATE (DD-MM-YYYY) 26-03-2015		2. REPORT TYPE Master's Thesis	3. DATES COVERED (From — To) October 2014 – March 2015	
4. TITLE AND SUBTITLE <b>MULTIPLE DETECTOR OPTIMIZATION FOR HIDDEN RADIATION SOURCE DETECTION</b>		5a. CONTRACT NUMBER		
		5b. GRANT NUMBER		
		5c. PROGRAM ELEMENT NUMBER		
6. AUTHOR(S)  Morrison, Michael MAJ, U.S. Army		5d. PROJECT NUMBER		
		5e. TASK NUMBER		
		5f. WORK UNIT NUMBER		
7. PERFORMING ORGANIZATION NAME(S) AND ADDRESS(ES) Air Force Institute of Technology Graduate School of Engineering and Management (AFIT/ENP) 2950 Hobson Way WPAFB OH 45433-7765		8. PERFORMING ORGANIZATION REPORT NUMBER AFIT-ENP-MS-15-M-082		
9. SPONSORING / MONITORING AGENCY NAME(S) AND ADDRESS(ES) Dr. David Petersen Defense Threat Reduction Agency DTRA-RD-BA 8725 John J. Kingman Rd Ft. Belvoir, VA 22060 (703) 767-3164		10. SPONSOR/MONITOR'S ACRONYM(S) DTRA		
		11. SPONSOR/MONITOR'S REPORT NUMBER(S)		
12. DISTRIBUTION / AVAILABILITY STATEMENT Distribution Statement A. Approved for Public Release; Distribution Unlimited				
13. SUPPLEMENTARY NOTES This material is declared a work of the U.S. Government and is not subject to copyright protection in the United States.				
14. ABSTRACT The purpose of this research was to demonstrate two things: the first, a validation of the 2 dimensional point attenuation kernel against the MCNP model for optimal placement of multiple NaI detectors. The second was to develop a model to deduce an employment/emplacement strategy for optimal detector placement based on the amount of devices available. The 2 dimensional model is able to replicate the MCNP results in a fraction of the time. Additionally, the point attenuation kernel can predict optimal detector locations with the same proficiency as the MCNP model.				
15. SUBJECT TERMS Optimization of NaI detector response				
16. SECURITY CLASSIFICATION OF:		17. LIMITATION OF ABSTRACT UU	18. NUMBER OF PAGES 83	19a. NAME OF RESPONSIBLE PERSON Justin Clinton, AFIT/ENP
a. REPORT U	b. ABSTRACT U	c. THIS PAGE U		19b. TELEPHONE NUMBER (Include Area Code) (937)255-3636, ext 4586